Single-Cell Resolution of Cellular Damage Illuminates Disease Progression

Tsimafei Padvitski[1,*], Paula Unger Avila[1,*], He Chen[2,3,*], Cem Özel[2,3], Fabian Braun[4,5,6], Roman-Ulrich Müller[1,2,3], Pål O. Westermark[6,7], Paul T. Brinkkötter[2,3], Bernhard Schermer[1,2,3], Thomas Benzing[1,2,3], F. Thomas Wunderlich[8], Martin Kann[2,3,#], Andreas Beyer[1,9,10,#]

Affiliations:

1. Cologne Excellence Cluster on Cellular Stress Responses in Age-Associated Diseases (CECAD), University of Cologne, Cologne, Germany.
2. Department II of Internal Medicine, University of Cologne, Faculty of Medicine and University Hospital Cologne, Cologne, Germany.
3. Center for Molecular Medicine Cologne, Faculty of Medicine and University Hospital Cologne, University of Cologne, 50931 Cologne, Germany.
4. III. Department of Medicine, University Medical Center Hamburg-Eppendorf, Hamburg, Germany
5. Hamburg Center for Kidney Health, University Medical Center Hamburg-Eppendorf, Hamburg, Germany
6. Martin Zeitz Center for Rare Diseases, University Medical Center Hamburg-Eppendorf, Hamburg, Germany
7. Working group Husbandry & Health, Research Institute for Farm Animal Biology (FBN), Dummerstorf, Germany
8. Institute for Biostatistics and Informatics in Medicine and Ageing Research, Rostock University Medical Center, Rostock, Germany
9. Max Planck Institute for Metabolism Research, Cologne, Germany.
10. Institute for Genetics, Faculty of Mathematics and Natural Sciences, University of Cologne, 50923 Cologne, Germany.

* These authors contributed equally

[#] Correspondence should be addressed to:

martin.kann@uk-koeln.de

andreas.beyer@uni-koeln.de

Abbreviations

AFLD: alcoholic fatty liver disease

NAFLD: non-alcoholic fatty liver disease

NASH: non-alcoholic steatohepatitis

ASH: alcoholic steatohepatitis

CCl4: carbon tetrachloride

HCC: hepatocellular carcinoma

HFD: high fat diet

scRNA-seq: single cell RNA sequencing

snRNA-seq: single nucleus RNA sequencing

CKD: chronic kidney disease

FSGS: focal and segmental glomerulosclerosis

PDS: podocyte damage score

HDS: hepatocyte damage score

Summary

Degenerative diseases are marked by the progressive accumulation of cellular damage, leading to impaired cellular function and tissue degeneration. Despite advances in single-cell technologies, capturing the gradual decline of individual cells *in vivo* remains challenging. Here, we present a novel, universal, cross-model framework for quantifying cellular damage at single-cell resolution, to uncover conserved molecular trajectories of cellular degeneration. This method uses single-cell RNA sequencing data and enables the detection of progressive damage within distinct cell populations under physiological and pathological conditions. We developed the Podocyte Damage Score (PDS) and Hepatocyte Damage Score (HDS) to monitor cellular deterioration in murine models of kidney glomerulosclerosis and liver steatosis, respectively. The application of these scores to both murine and human datasets accurately quantified cellular damage across diverse disease models and distinguished varying degrees of damage even in unperturbed samples. Notably, the PDS revealed circadian gene expression dysregulation as a hallmark of podocyte injury, while the HDS identified a critical threshold of hepatocyte damage leading to cellular senescence and metabolic dysfunction. The approach provides a scalable tool for decoding disease progression and identifying therapeutic targets across degenerative disorders.

Introduction

Degenerative diseases, such as chronic kidney disease (CKD) and non-alcoholic fatty liver disease (NAFLD), represent a growing global health burden. The global prevalence of CKD in 2010 was estimated at ~11%[1], and non-alcoholic fatty liver disease (NAFLD) was considered to affect ~25% of the global population in 2016[2]. These conditions are characterized by the gradual accumulation of cellular damage, leading to progressive loss of tissue function and contributing to severe complications, including organ failure and cancer. Despite their prevalence, the molecular mechanisms that drive the onset and progression of degenerative diseases remain poorly understood. This knowledge gap hampers the development of targeted diagnostics and effective therapies. A central challenge in studying degenerative diseases lies in capturing the slow and heterogeneous progression of cellular dysfunction. Disease onset often involves subtle, progressive changes within specific cell populations that are difficult to detect using conventional bulk analyses or histopathology. Moreover, existing animal models frequently mimic rare, monogenic forms of disease and fail to reflect the complexity of sporadic, multifactorial conditions in humans.

In CKD, the progressive decline of kidney function almost invariably involves damage to podocytes, terminally differentiated epithelial cells within the kidney glomeruli, the filtration units of the kidney. However, recent large-scale transcriptomic approaches in humans have shown that changes in glomerular transcriptional programs, while depicting individual aspects of CKD secondary changes, cannot explain the gradual progress of podocyte degeneration[3–7]. Similarly, NAFLD involves a complex interplay between liver cell types, while its defining criterion is damage to the predominant hepatic epithelial cell type, the hepatocyte[2]. Hepatocytes are key to metabolic functions of the liver and are tightly connected to inflammatory and immune responses. However, pathways of gradual degeneration and ultimately carcinogenesis are still elusive [8,9].

Advances in single-cell RNA sequencing (scRNA-seq) have revolutionized our ability to profile gene expression at cellular resolution, offering new opportunities to dissect disease processes at unprecedented detail and study the function of disease-associated genes[10] and regulatory events[11]. However, current analytical approaches are limited in their capacity to quantify gradual cellular deterioration. Traditional clustering and differential expression analyses primarily capture discrete cell states, overlooking continuous damage progression. Pseudo-time trajectory methods, while useful for modeling developmental processes, often struggle to distinguish between physiological variability and pathological decline.

To address this gap, we introduce a novel computational framework for quantifying cellular damage at single-cell resolution. By developing cell-type-specific damage scores - namely, the Podocyte Damage Score (PDS) and Hepatocyte Damage Score (HDS) - we systematically track molecular deterioration in kidney and liver disease models. These scores, for the first time, represent *in vivo* states of cells in chronic disease over extended time periods and enable the identification of molecular pathways associated with progressive damage, even within rare or early-stage diseased cells. Applying this framework across diverse murine models and human datasets, we uncover conserved mechanisms of cellular injury, including disrupted circadian rhythm in podocytes and senescence-driven metabolic dysfunction in hepatocytes.

Our approach is transferrable to other chronic diseases and offers a powerful tool for mapping cellular damage trajectories, providing critical insights into disease progression as well as potential therapeutic targets across degenerative conditions.

Results

Damage scores

Cellular damage can be defined in different ways. Here, we pursue an operational definition of ‘cellular damage’ by defining cellular damage as a pathological cellular state that is not specific to one particular disease-causing mechanism. Instead, damage is a common, pathological cellular state resulting from a broader spectrum of disease entities, disease-causing mechanisms, and/or a loss of homeostasis. Such cell-type specific cellular damage states are well established in histopathology. Here, we develop an approach for the molecular characterization of such states. To demonstrate the general applicability of our concept, we developed two single-cell damage scores: one for podocytes (Podocyte Damage Score, PDS), to track damage during the progression of CKD, and a second for hepatocytes (Hepatocyte Damage Score, HDS), to explore progressive damage in chronic liver pathologies such AFLD and NAFLD. In the following, we first motivate the selection criteria for damage marker genes and subsequently validate both scores using mouse and human single-cell and spatial omics data. Finally, we present applications of first the PDS and then the HDS to demonstrate the added value and novel mechanistic insight gained from these scores.

The key notion of our approach is to identify marker genes whose expression is associated with increasing damage across a wide range of disease models (Fig. 1a). By combining diverse

disease models in the selection process, we ensure that the marker genes are not just markers for one specific intervention, but report on damage of the target cell type in general. Further, our approach ensures that selected marker genes are expressed in the target cell type, thereby excluding for example genes specific to tissue-resident immune cells that might be indicative of inflammation. Using gene expression data from 37 datasets covering 9 podocytopathy models and ~250 samples covering 13 liver disease models (Supplementary Table 1), we first ranked genes by their p-values for differential expression in each of these models (always comparing the diseased/experimental condition versus the respective control). Those ranks were subsequently averaged across all disease models per cell type to obtain one global gene ranking for podocytes and one for hepatocytes. Next, we applied two additional filters: first, we removed genes that were not expressed in the target cell type (i.e. podocytes or hepatocytes; Methods). Second, we only kept genes with a consistent direction of change (same sign) in at least 75% of all studies. Finally, we chose the top *n* genes as damage marker genes for each of the two cell types. To quantify the damage of an individual cell (or bulk sample), we tested how extreme the expression of PDS/HDS marker genes was in a given cell using AUCell[12]. Genes with positive and negative log-fold changes were combined considering the direction of effects (Methods), resulting in an algorithm capable of scoring cellular damage at single cell resolution (Fig. 1b,e).

Damage scores robustly characterize cellular states

To establish the robustness of our approach, we first confirmed that varying the number of top genes used for the damage scores had little influence on the outcome. Varying the number of maker genes between 20 to 200 genes only minimally affected the scores' ability to distinguish (diseased) experimental samples from (healthy) control samples (Supplementary Fig. 1a,b). Likewise, randomizing parts of the input data had little influence on the ability of the damage scores to distinguish healthy from diseased samples. Even when randomizing (shuffling) up to 70% of all input studies, the resulting damage scores were still able to distinguish experimental from control samples in disease models that were not used for developing the damage scores (Supplementary Fig. 1c,d). The choice of the top *n* genes used for computing the damage scores is, to an extent, arbitrary. We decided to continue all subsequent work with the top 42 marker genes for each, PDS and HDS (Supplementary Table 2). Next, we confirmed that the PDS was indeed cell-type specific. By analyzing snRNA-seq data obtained from glomeruli, we confirmed that only the targeted cell-type showed significant variation with damage (Supplementary Fig. 1e). Furthermore, available glomerular proteomic data[13] confirmed that PDS marker proteins were

more abundant in podocytes compared to mesangial and glomerular endothelial cells (Supplementary Fig. 2a).

A central aim of our study was to develop scores that measure cellular damage across disease conditions instead of reflecting molecular adaptations in specific disease models. We tested this notion using a 'leave one model out' cross validation: first we removed all samples of one similar group of disease models from the training data, then performed the procedure described above to determine damage marker genes on the remaining samples and, finally, tested the resulting damage scores on the left-out disease model samples. In each of the cross-validation rounds, both the PDS and HDs were able to distinguish experimental samples from control samples in the unseen disease models (Fig. 1c,f and Supplementary Fig. 2b-e). Altogether, these results demonstrated that the damage scores are remarkably robust against diverse variations in the data and that they capture generic molecular changes operating across disease models in a cell-type specific fashion.

Damage coincides with declining cellular identity

Most marker genes for PDS and HDS were downregulated with increasing damage (PDS: 39/42, HDS 30/42, Supplementary Table 2), suggesting a loss of cell type-specific gene expression. Downregulated PDS markers included genes with established key roles in podocyte biology, such as genes coding for the slit diaphragm-associated regulators Magi2, Thsd7a, Robo2, and Ddn [14–16]. Further, mutations in the PDS genes Plce1, Wt1, Magi2, and Ptpro are known to cause podocytopathies in humans[14,17–19]. Other PDS genes with established function in podocytes include the transcription factors (TF) Mafb and Dach1, as well as Sulf1, Cldn5, Optn, Pard3b, Enpep, and Sema3g[20–25]. Overall, PDS genes were enriched for pathways with high relevance to podocyte biology (Supplementary Fig. 2f).

Likewise, many HDS marker genes downregulated in the disease condition are involved in hepatocyte-specific functions such as bile acid metabolism (e.g. Cyp7b1[26]), detoxification (e.g. Selenbp2[27]) and factors secreted into the blood (e.g. Serpinc1 i.e., antithrombin[28] and C8b[28]). Further, downregulated HDS marker genes are involved in the maintenance of cellular homeostasis, for example, maintaining genomic stability (e.g. Mcm10[29]), response to oxidative stress (e.g., Mvpv17l[30]), and immuneregulation (e.g. Ddt[31]). Other negative HDS genes have previously been associated with the progression of liver disease (e.g. Nudt7[32], Hes6[33]), as well as with impaired liver regeneration (e.g. Lifr[34] and Tm7sf2[35]).

Upregulated HDS genes were active in fatty acid uptake (e.g. Cd36[36]), suppression of gluconeogenesis (e.g. Nrg1[37]), and lipid transport (e.g. Apoa4[38]), and were significantly enriched for pathways relevant to cell-adhesion and wound healing processes, indicating responses to tissue damage (Supplementary Table 3). Examples are Rtn4, which activates TGFβ-mediated fibrosis[39], as well as Iqgap1, which has already been shown to positively correlate with damage. In line with this evidence, silencing Iqgap1 ameliorates hepatic fibrogenesis[40], and suppresses liver cancer[41]. Taken together these results suggest that cellular damage in podocytes and hepatocytes proceeds in conjunction with cell identity loss[42,43].

PDS and HDS report on pathologic cellular states

Morphological validation

To validate the association of the PDS with histologically detectable damage, we used two morphological features: first, we used glomerular size, because glomerular hyperfiltration such as in diabetic kidney disease results in glomerular hypertrophy and consecutive podocyte stress, as podocytes are unable to divide for compensation[44,45]. Thus, larger glomeruli are indicative of greater podocyte damage. Second, we used the slit diaphragm (SD) length, which is a proxy for damage to the podocyte filtration barrier, with shorter length indicating greater damage[46]. We used spatial transcriptomic data from diabetic mouse kidneys and controls[45] to correlate glomerular area and glomerular PDS normalized for area. We observed a significant correlation ($p < 1x10^{-4}$ in controls, $p < 1x10^{-10}$ in diabetic mice) between the two measures (Fig. 1d, Supplementary Fig. 3a), showing that the PDS captures within sample variability of cellular damage. Importantly, PDS indicates that glomerular size in wildtype mice is associated with podocyte stress presumably attributable to increased filtration load. Second, we used STED imaging of SDs to assess the protein expression of several PDS signature members localizing to the SD, namely THSD7A, CLDN5, and EPHB1. This confirmed decreased (EPHB1, THSD7A) or redistributed signals (CLDN5) with shortened SDs in podocytopathy models as compared to controls, consistent with the expected changes from PDS gene expression analyses (Supplementary Fig. 3b). In conclusion, morphological aspects of podocyte disease align with the PDS.

In the liver, a unifying, histologically detectable and locally heterogeneous feature of many disease conditions including viral hepatitis, AFLD, and NAFLD, is the ectopic formation and accumulation of lipid droplets in hepatocytes (also called liver steatosis)[47]. Therefore, we

assessed the local accumulation of lipid droplets in hepatocytes as a proxy for accumulated hepatocyte damage. Using spatial transcriptomic data from a cohort of NAFLD mice and healthy controls[9,48], we confirmed that the HDS captured within sample variation of liver tissue damage. First, we observed significantly lower average HDS in healthy control liver sections when compared to liver sections from NAFLD mice (Supplementary Fig. 3c). Importantly, within the same tissue section from NAFLD mice, areas with more abundant fat droplets had greater HDS than less lipid-laden areas (Fig. 1g, Supplementary Fig. 3d). Taken together, these results confirm that the PDS and HDS marker genes are indicative of histologically detectable damage.

Functional validation

To test if the PDS also reflects functional decline of podocytes, we correlated the PDS with albuminuria measurements in mice. The albumin/creatinine ratio (ACR) quantifies excess proteins in the urine and is a quantitative and established measure of podocyte damage[49,46]. We analyzed 12 mouse studies with combined bulk glomerular transcriptomic and ACR measurements and found a significant positive correlation (Spearman=0.45) between PDS and albuminuria (Supplementary Fig. 4a). The correlation was even stronger (Spearman=0.89) for novel snRNA-seq data generated within this study (Fig. 2a, Supplementary Fig. 5). Here, we aggregated PDS across podocytes within each sample and then correlated these pseudo-bulk PDS with albuminuria (Fig. 2a). Taken together, these results indicate that PDS quantitatively reflects functional decline of podocytes. In some contexts, the PDS may even replace albuminuria as a surrogate measure of podocyte damage, because unlike albuminuria it is measurable outside of a functioning organism and even in single cells.

PDS and HDS are predictive in human data

PDS and HDS were developed using exclusively murine transcriptomic data and revealed very robust gene signatures. Hence, we asked next whether the signature was conserved in and therefore applicable to human data as well. To this end, where available, we identified the unambiguous one-to-one human orthologues of all murine genes constituting the signatures. For the PDS, we re-analyzed publicly available human data from the Kidney Precision Medicine Project (KPMP)[3], including patient clinical characteristics, histology, sc/snRNA-seq data, and spatial transcriptomics. To test the clinical predictive value of the PDS in humans, we correlated human ACR with the PDS and other established clinical predictors of albuminuria such as age, sex, diabetic status across the KPMP cohort. Only diabetic status and the PDS were significantly correlated with ACR (Fig. 2b, Supplementary Fig. 4b), thereby replicating the findings obtained in

mice. Within the KPMP spatial transcriptomic dataset, we identified a biopsy core clearly showing an FSGS phenotype. Within this sample, PDS correlated with histologic features of FSGS distinguishing healthy from sclerosed glomeruli and even resolving segmental glomerulosclerosis within a single glomerulus (Fig. 2c, Supplementary Fig. 4c). In addition, when we computed the PDS on scRNA-seq data of podocytes that were recovered from human urine within the NEPTUNE study[50], PDS correlated with the urine protein/creatinine ratios (UPCR) at the time of urine collection (Supplementary Fig. 4d). Finally, in microarray, bulk RNA-seq, and snRNA-seq data of human kidney biopsies, the PDS clearly distinguished healthy control subjects from patients suffering from primary FSGS, IgA nephropathy, and chronic kidney disease, respectively[3,7,51] (Supplementary Fig. 4e). To conclude, a human ortholog-based PDS was readily capable of discriminating functional and morphological features of human podocytopathies.

In a parallel approach for the HDS, a total of 34 HDS marker genes had one-to-one orthologs in humans. Using these orthologs, we calculated the HDS on hepatocytes of snRNA-seq human liver samples[52]. The HDS readily differentiated three healthy control subjects from three patients suffering from NASH (Fig. 2d). Taken together, our findings indicate that conserved cell-type specific damage scores can be developed from murine transcriptomic data that are subsequently amenable to translational application in humans.

Comparison of HDS and trajectory inference

Pseudo-time trajectories have been proposed as an alternative approach for the computational alignment of single-cell and single-nucleus data along developmental, spatial and temporal gradients[53]. Compared to the single-cell damage scores presented here, pseudo-time trajectories have potentially two disadvantages: first, they are not readily applicable across different studies, disease models and species as pseudo-time trajectories are commonly inferred per dataset or per study after appropriate data integration. Second, pseudo-time trajectories may have a disadvantage if gradients in single-cell data are dominated by signals other than cellular damage. An example is liver zonation: gene expression in hepatocytes is strongly determined by their relative position with respect to periportal and central veins, a signal that potentially ‘shades’ expression changes caused by cellular damage. To test this notion, we compared a semi-supervised method for pseudo-time trajectory inference (TSCAN[54]) to the HDS. Applying both algorithms to hepatocyte snRNA-seq data from mice suffering from NAFLD and controls, for which zonation information was available at individual hepatocyte level[52], we confirmed that the HDS separated undamaged from damaged hepatocytes independent of their zone of origin (Fig. 2e), i.e. the HDS is independent of liver zonation. As opposed to that, the pseudo-time trajectory was

dominated by gene expression patterns driven by hepatocyte zonation (Fig. 2f, Supplementary Fig. 4f). Thus, the damage scores presented here provide information that is distinct from and complementary to pseudo-time trajectories.

Characterizing cellular changes during disease progression

Pathway signatures reveal altered metabolism in damaged podocytes

Having validated our scores, we next sought to leverage their potential in addressing unanswered questions in kidney and liver biology. A key feature of the single-cell damage scores developed here is that they facilitate the analysis of progressive molecular changes associated with increasing cellular damage in disease models and even under unperturbed control conditions. To implement this notion, we developed a scheme that first sorts cells *in silico* along a damage trajectory from low to high damage and next identifies regulatory pathways and cellular processes (subsequently collectively called 'pathways') whose activity changes progressively along this axis. Cells with similar damage scores were binned (grouped) to reduce noise, and pathway activities per bin were determined using AUCell (Methods) for all KEGG and Reactome pathways. We note that this approach does not compare gene expression variation between samples, which runs the risk of being affected by batch effects and other inter-individual variation. Instead, this scheme enables the analysis of disease progression within a single sample. Importantly, cells from control samples also displayed a spectrum of damage. Even though the average damage was lower in control samples compared to the experimental conditions, such samples always contained a small fraction of cells with relatively high damage scores (Fig. 1b,e, 3a). This observation motivated us to sort cells by damage within the control samples and identify pathway activity changes along this gradient of otherwise unperturbed cells. Thereby, it became possible to identify pathway activity changes that were consistently changing in the same direction between experimental and control conditions, which can be considered general components of cellular damage and less likely attributable to a specific disease model or trigger. This approach allowed for addressing a key conundrum in the diagnostic approach to glomerular kidney disease, i.e., the contrast between a uniform histologic phenotype of podocyte damage – FSGS – and the multiple triggers, diseases and molecular pathways resulting in this phenotype. First, this poses a clinical challenge, as histology is often insufficient to provide a conclusive diagnosis. Second, it remained

challenging to differentiate common from trigger-specific cellular events leading to the FSGS phenotype.

To address this challenge, we obtained published glomerular scRNA-seq data for four podocytopathy models[55], and generated snRNA-seq data for another three models (Supplementary Fig. 5) to reflect a wide range of podocyte damage triggers relevant to important aspects of podocyte biology as well as clinical settings. Together these models include mutations in slit diaphragm proteins (Nphs2^{mut}, Cd2ap^{pko}), metabolic and oxidative stress (Pdss2^{mut}, doxorubicin), antibody-mediated glomerular inflammation (NTN), diabetes (Btbr$^{ob/ob}$), and mutation of a key podocyte transcription factor (Wt1$^{ko/wt}$, Supplementary Table 4). Next, we quantified pathway activity changes along the PDS axis as outlined above and focused on pathways that are either already known to be relevant to podocyte biology or changed highly dynamically with increasing damage. This way, we established 'pathway fingerprints' that characterize the regulatory, cell structural and metabolic changes happening during progressively increasing damage in a specific disease model (Fig. 3a,b, Supplementary Fig. 6). These pathway fingerprints provide a rich source of information, allowing us to discern common and unique patterns of pathway changes across disease models. First, pathways that were expected to show model-specific behavior due to the nature of various damage triggers distinguished fingerprints from each other. For example, in a complex with NPHS2 (podocin), tight junction proteins are part of the slit diaphragm protein complex[56,57], and the tight junction pathway within the fingerprint of the podocin mutation model expectedly distinguished this model from others (Fig. 3a). Similarly, mutating the mitochondrial regulator Pdss2 was reflected by specific activity changes of the closely associated mitochondrial pathway 'thermogenesis'. In addition to highlighting model-specific pathways, fingerprints also established pathways commonly modulated with podocyte injury and independent of the trigger. For example, hippo signaling, which was initially found downstream of Wt1 transcriptional regulatory function in podocytes[17], was now shown to be unequivocally decreased upon podocyte damage in all models. Key pathways in podocyte biology related to the actin cytoskeleton, cell adhesions or the renin angiotensin system were also commonly modulated (Fig. 3a). In addition to cell structural and regulatory changes, we also observed common metabolic changes of podocytes that were associated with increasing damage. Energy metabolism (glycolysis and oxidative phosphorylation) and protein production (translation) were consistently upregulated with increasing damage across models, suggesting that podocytes are majorly reorganizing their proteome while changing their shape and coping with increasing stress.

In the clinical context, albuminuria is used as a measure to 'align' the disease status between patients. Here, we test if the PDS could serve a similar purpose for 'aligning' cellular damage states across disease models. Therefore, we integrated damage levels as indicated by the PDS with pathway activity changes across disease models (Fig. 3b). This approach allows for aligning and directly comparing multiple disease models, samples or patient biopsies with respect to damage levels and associated signaling pathway behavior. Here, ephrin signaling, which was recently identified as a pathway relevant to progression of kidney disease[58] was consistently downregulated upon podocyte damage. To experimentally test the relevance of ephrin signaling in the context of podocyte damage, we performed fluorescent labelling and STED imaging of Ephrin type-B receptor 1 (Ephb1), which is one of the PDS marker genes (Supplementary Fig. 3b). This analysis confirmed the localization of Ephb1 to the slit diaphragm and showed substantial depletion in damaged podocytes. In summary, pathway fingerprints and damage trajectories identified trigger-specific as well as commonly regulated pathways upon podocyte damage, rendering the PDS suitable for molecular diagnostic approaches to FSGS and for resolving its molecular etiology.

Identifying generic druggable targets with the PDS

A curious result of our pathway fingerprint analysis was the aberrant and model-specific behavior of the pathways "Focal adhesion" and "Regulation of actin cytoskeleton" in the Nphs2^{mut} model when compared to all other models (Fig. 3a). Focal adhesions attach podocytes to the glomerular basement membrane (GBM), making them a crucial organelle to the GBM detachment of podocytes during FSGS[56,57]. Focal adhesions and the slit diaphragm are further tightly connected to the actin cytoskeleton, which is commonly modulated and rearranged upon podocyte damage[59]. A key morphological feature associated with this rearrangement is foot process effacement. We therefore utilized the PDS to gain deeper insight into the reorganization of the 'podocyte adhesome' upon damage.

We correlated the expression of members of the podocyte adhesome[60] with the PDS in each of the disease models and control samples (Fig. 3c). Selected members of this network were distinctly regulated in the Nphs2^{mut} model compared to all other models. For example, two genes encoding for actin binding proteins, dystonin (Dst) and palladin (Palld), exhibited strong negative correlations with the PDS in the Nphs2^{mut} model, whereas in other disease models they were uncorrelated or even oppositely correlated with the PDS (Fig. 3c). These examples underline the importance of distinguishing model-specific changes that potentially act upstream of podocyte damage from alterations that are consistent across models. Therefore, we next identified

adhesome components that were consistently downregulated with increasing damage irrespective of the damage trigger. These components included the actin binding molecules Parva and Epb41l5, the extracellular matrix receptors Itgb5 and Itga3, the cell surface peptidase Dpp4, and the kinase Pak1 (RAC1 activated kinase 1). All of these components had previously been identified as relevant to podocyte focal adhesion function[60–63]. Parva and Epb41l5 in particular have been shown to prevent podocyte detachment from the GBM in FSGS[61,62]. Pak1 is a key regulator of the focal adhesion and actin cytoskeleton networks and has been shown to be involved in the earliest events of FSGS in a CTCF deletion model[64]. Further, our work surprisingly reveals that downregulation of the cell-surface peptidase Dpp4 (dipeptidyl peptidase-4) is a hallmark of increasing podocyte damage across disease models, including diabetes. Dpp4 has been reported as upregulated in diabetes in a number of tissues and cell types and contributes to decreased insulin sensitivity. In podocytes, Dpp4 physically interacts with the focal adhesion protein integrin beta-1 (Itgb1)[65], and Dpp4 inhibitors decrease albuminuria in mouse models of podocyte damage[66]. These drugs are a mainstay in the treatment of type 2 diabetes mellitus, where their use was associated with beneficial albuminuria outcomes in several clinical trials[67–70]. Taken together, the surprising downregulation of Dpp4 in seven independent disease models can be interpreted as a repair response amenable to preventative treatment. Thus, our integrative adhesome and PDS network analysis revealed promising targets for the prevention of podocyte GBM detachment in podocytopathies.

Transcriptional networks driving podocyte damage

Regulators of podocyte gene expression drive cross-model correlates of the PDS

To better understand the regulatory programs driving the expression changes of genes relevant to the podocyte damage response, we constructed a podocyte-specific transcription regulatory network (TRN) (Fig. 4a). To derive this TRN, we acquired podocyte-specific ATAC-seq data by FACS-sorting podocyte nuclei from a nuclear GFP reporter mouse (Methods, Supplementary Fig. 7a). Next, we performed foot-printing and transcription factor (TF) motif scanning within accessible chromatin regions, using DNA binding motifs of 110 TFs that were expressed in podocytes. Finally, we grouped TFs with very similar DNA binding motifs into 14 TF families, as their binding signatures were difficult to distinguish without further information (Supplementary Fig. 7b). We combined predicted target genes of all motifs within each cluster, forming a TF

regulon, and named each regulon after a representative transcription factor (Supplementary Fig. 7c). This established a network between 14 TF families and 6,360 target genes expressed in podocytes that will serve as a critical resource also for future research into podocyte biology.

To systematically identify target genes of these regulons that were involved in FSGS progression across models, we computed how often a gene was correlated with the PDS across snRNA-seq studies of FSGS, in both experimental and control conditions. Note that this detection of commonly perturbed genes in experimental and control conditions cannot be achieved with traditional differential expression analysis, but necessarily requires a within-sample trajectory analysis[71]. Based on these results we selected 152 genes that were significantly correlated (Supplementary Table 5, t-test, adjusted p-value < 0.1) with the PDS in seven or more tests. Forty of those genes were already members of the PDS marker gene set.

This set of 152 genes contained eight podocyte-expressed TFs, i.e. out of the 110 TFs that were used to create the TRN. Thus, we used the TRN to inspect the regulatory relationships among these eight TFs that were tightly associated with podocyte damage (Fig. 4a). These TF genes included the core podocyte TFs Wt1, Mafb, and Tcf21, TFs known to respond to external damage cues (Egr1, Fos), and TFs with as yet uncharacterized functions in podocytes (Zbtb20, Zfp423, Creb3l2). The regulators established two groups: one group of regulators controlling all of the eight PDS-associated TFs and another set of regulators only controlling four of them (Egr1, Wt1, Mafb, Zbtb20). Confirming previous studies, we identified the regulons for the Wt1-, Lmx1b-, and Tead1-families as controlling the majority of TF genes correlating with the PDS[17]. Interestingly, in addition to these established podocyte regulons, the Irf1, Nr1d1, and Rela families were similarly prominent, indicating that inflammatory signals and processes dependent on nuclear receptor signaling such as the circadian clock may be relevant to podocytes damage (Fig. 4a)[71].

Podocyte damage disrupts the circadian clock

Next, we utilized the podocyte TRN to identify potential regulators of genes that were likely involved in podocyte damage either because their own expression correlated with the PDS (i.e. the 152 genes from above) or because they are involved in cellular functions that are known to be relevant for podocytopathies, like the podocyte adhesome[60], matrisome[72], actin cytoskeleton[73], and slit diaphragm[57]. Consistent with earlier work we found that Wt1 was predicted to bind regulatory elements of the majority of genes involved in these key podocyte structures as well as of genes correlating with the PDS (Fig. 4b). Next to Wt1, the TF families containing Rela and Irf1 (both of which are reacting to inflammatory stress) were prominent regulators of these damage-

associated gene sets. Further, all gene sets were co-regulated by a combination of cell type-specific podocyte TFs (e.g. Wt1, Lmx1b, Foxc1, Mafb, Tcf21) and generic TFs (e.g. Tead1, AP-1 complex / Fos, Supplementary Fig. 7d). The fact that some of the generic regulators were themselves correlated with the PDS (e.g. Fos) is suggesting that the transcriptional response to podocyte damage is coordinated via an intricate network of generic and cell type-specific TFs (Supplementary Fig. 7c). A striking finding was that nuclear receptor subfamily 1 group D (Nr1d1, Rev-Erb alpha) was predicted to regulate a wide range of genes that we found to be correlated with the PDS (Fig. 4b). Rev-Erb alpha is one of the core TFs regulating feedback loops within the intracellular circadian clock[74], and is instrumental in establishing circadian gene expression. Recent studies have established that many key podocyte genes are expressed in a circadian fashion and that the disruption of the podocyte circadian clock results in podocyte dysfunction[75–77]. Based on the tight link between Nr1d1 and many of the PDS-associated processes across disease models, we speculated that the reverse may also be true, i.e. that podocyte damage interferes with the circadian clock. To experimentally validate this link, we first generated circadian gene expression data from whole murine kidneys by performing transcriptomic profiling in 3-hour time intervals over a 48-hour period. Using this data, we determined genes with circadian expression oscillation and intersected this gene list with podocyte expression data to obtain a set of genes with circadian expression in podocytes (Methods, Supplementary Fig. 8). This gene set was indeed significantly enriched in podocyte Nr1d1 target genes as determined in our TRN (Fig. 4b).

We then asked if increasing podocyte damage as measured by the PDS was associated with increased disruption of circadian gene expression. To this end, we employed two different methods to determine disruption of circadian gene expression in single cells – TEMPO[78], which determines average time shifts between the expression of core clock genes and other circadian genes, and CRD[79], which measures the variance among circadian genes. Here, we fully exploited the single-cell capacity of our score as damage-dependent circadian expression heterogeneity was captured within one sample, with the organism being normalized for all common factors potentially affecting circadian rhythms such as cortisol levels, organism redox state, time of day, blood pressure etc. Both approaches revealed that increased podocyte damage correlated with increased disruption of circadian gene expression within sample, an effect that was shown across podocytopathy models (Fig. 4c,d). In conclusion, disruption of circadian gene expression appears to be a common consequence of podocyte damage. Given the large number of essential podocyte transcripts exhibiting circadian oscillation[75], this finding bears significant relevance to

understanding podocyte damage. Further, given that disruption of the clock and hence circadian gene expression results in podocyte damage[76], and podocyte damage results in disruption of circadian gene expression, positive feedback loops contributing to podocyte damage by means of this mechanism appear likely (Fig. 4e). In summary, our integrative analysis of the PDS together with the TRN have yielded important insights into mechanisms of podocyte damage.

HDS reveals metabolically distinct cell fate trajectories of damaged hepatocytes

Accumulation of damage can drive hepatocytes into highly distinct cellular states, including neoplastic transformation (i.e. establishing hepatocellular carcinoma, HCC), cell death, and senescence[80,81]. Since the pathophysiological role of senescent hepatocytes in chronic liver disease has not been widely investigated nor fully understood, we focused specifically on the transition of healthy hepatocytes into this cell state[80]. To explore this cell fate transition, we used hepatocyte snRNA-seq data from mice at two different ages (3-month-old and 9-month-old) fed with a NASH-inducing diet or a control diet respectively[52]. To quantify the senescence status of hepatocytes we used the SenMayo marker gene set[81]. First, we evaluated the senescence status of cells in relation to the HDS and observed a clear increase of senescent cells with increasing cellular damage (Fig. 5a,b). This analysis revealed a 'tipping point': until an HDS of about -0.05 we did not observe any noticeable increase in the number of senescent cells. However, beyond that damage level cells increasingly adopted a senescent-like state (Fig. 5b). Further, cells started to adopt divergent cell states with increasing HDS. Although a large fraction of cells became increasingly more senescent-like, many other cells were able to maintain a low senescence score despite being substantially damaged according to their HDS. To formally quantify this notion, we computed the inter quartile range (IQR) of the range of senescence scores as a function of the HDS, which revealed a substantial increase of the IQR after the same tipping point (HDS $\approx$–0.05; Fig. 5b). Thus, these findings support the notion that damaged hepatocytes develop along divergent trajectories towards distinct cellular fates, one of them being cellular senescence. While cellular damage beyond a certain threshold seems to be a necessary requirement for the entry into the senescent state, that cell fate decision does not seem to be fully deterministic, as a large fraction of highly damaged hepatocytes escapes entry into senescence.

To determine the transcriptional alterations associated with these cell fate transitions, we grouped cells into the following classes using the HDS and the senescence score: undamaged hepatocytes (low HDS), damaged hepatocytes (high HDS), and cells in a transition state with

intermediate HDS. Damaged cells were further sub-classified as ‘senescent’, ‘non-senescent’ or 'unresolved’ depending on their senescence score (see Methods for details).

The relative abundances of hepatocytes in each cell fate category varied greatly with disease progression (Fig. 5c). First, we observed a sharp increase of the fraction of damaged hepatocytes with age: whereas more than 50% of hepatocytes from the 3-month-old control mouse were categorized as ‘undamaged’, the fraction of undamaged hepatocytes decreased to 25% in the 9-month-old control mouse. Further, the 3-month-old mouse fed NASH-inducing diet shared a very similar distribution of hepatocyte cellular fates compared to the 9-month-old control animal; transition hepatocytes became the dominating cell fate group in both cases, suggesting early signs of damage at the age of 3 months associated with the NASH-inducing diet. Even though the fraction of damaged hepatocytes was increased in both the 9-month-old control animal and the 3-month-old mouse with NASH-inducing diet, only a small fraction of these damaged cells in the latter mouse was classified as senescent. In contrast, the 9-month-old mouse fed a NASH-inducing diet showed a very distinct cell fate composition with over 75 % damaged hepatocytes and about 20% senescent-like hepatocytes (Fig. 5c).

To better characterize these cell fates, we determined genes that were differentially expressed between the senescent-like and not-senescent damaged hepatocytes. We found 37 genes with significantly increased expression and 210 genes with decreased expression in senescent-like damaged hepatocytes (adjusted $p < 0.05$, absolute $\log_2$(Fold Change) > 0.5, and expressed in at least 10% of senescent or not-senescent damaged hepatocytes). Out of the 37 genes significantly upregulated among the senescent cells, 14 were part of the SenMayo gene list.

Genes down-regulated in the senescent-like hepatocytes were enriched for functions related to hepatic metabolism, such as insulin signaling (e.g., Irs1[82] and Gpcpd1[83]), lipid catabolism (e.g., Nr1i3 and Prdx6), bile acid synthesis (e.g., Cyp7a1, Cyp27a1 and Sult2a8), as well as amino acid (e.g., Ahcy[84]) and xenobiotics breakdown (e.g., Cyp1a2[85]) (Fig. 5d, Supplementary Tables 6, 7). For example, the expression of *Cyp7a1* and *Cyp27a1,* that encode rate limiting enzymes of the canonical and alternative bile acid biosynthetic pathways, were first slightly upregulated with damage, but then drastically downregulated in senescent-like cells. A downstream effector of the bile acid synthesis pathway, the sulfotransferase Sult2a8, was slightly downregulated in not-senescent damaged hepatocytes, with a complete shutoff in senescent like hepatocytes. This enzyme is responsible for the detoxification of bile acids through sulfonation and is important for the maintenance of a homeostatic bile acid pool[86,87]. This downregulation of enzymes involved in bile acid biosynthesis in senescent-like cells was accompanied by an upregulation of genes

involved in ERK signaling (e.g., Nrg1, Vegfa, Igrf1 and C3, Fig. 5e), which has been associated with the suppression bile acid synthesis[88]. Taken together, these findings indicate that the bile acid metabolism in senescent hepatocytes may be much more compromised than in other damaged hepatocytes.

Several genes that are associated with hepatic steatosis were specifically upregulated in the senescent damaged hepatocytes (Fig. 5e, Supplementary Tables 6, 8). For example, we observed a strong induction of the gene encoding for secreted phosphoprotein 1 (Spp1). Spp1 (also known as osteopontin, OPN) inhibits autophagy, which accelerates lipid accumulation in the development of NAFLD and coincides with a senescent-like phenotype[89]. Further, silencing Spp1 in mice reduces lipid accumulation, while Spp1 over-expression attenuates steatosis[89,90]. Another example is Reticulon 4 (Rtn4 also known as Nogo) whose expression was also highly upregulated in senescent damaged hepatocytes and which has been linked to diet-induced fatty liver disease. Silencing Rtn4 has been shown to inhibit diet-induced fatty liver, insulin resistance and other aspects of metabolic disorder[91], while Rtn4 over-expression has been linked with decreased cancer survival and it has been associated with boosting tumorigenesis in the liver through the hyper activation of the Akt-pathway and a disruption of lipid homeostasis in mice[92].

With respect to lipid metabolism, we observed a dichotomous regulation of lipid anabolism and catabolism. The expression of genes involved in lipid biosynthesis and transport increased in damaged hepatocytes compared to undamaged hepatocytes independent of their senescent status (Fig. 5d). An example is Stearoyl-CoA desaturase 1 (SCD1)[93], which is a key regulator of lipid biosynthesis, that was upregulated in both senescent-like and not-senescent damaged hepatocytes. As opposed to that, genes involved in lipid catabolism, especially fatty acid oxidation, were specifically downregulated in senescent-like damaged hepatocytes (Fig. 5e). An example is Prdx6, which promotes fatty acid oxidation and whose suppression exacerbated hepatic steatosis in mice[94]. In line with this observation, we also observed a progressive down-regulation of the gene Nr1i3, which encodes for the Constitutive Androstane Receptor (CAR) along with the CAR target gene Cyp2c29[95,96] (Fig. 5e). CAR activation can drastically improve fatty liver disease and insulin signaling, while the loss of CAR associates with the accumulation of triglycerides in the liver[97–99].

In summary, our observations support a model in which cellular damage precedes the emergence of a senescent phenotype in hepatocytes and that the entry into this cell fate is in part a stochastic process. Further, senescent, and not-senescent damaged hepatocytes constitute two distinct

cellular fates that are metabolically highly divergent. The expression changes reported here may indicate senescent hepatocytes as key contributors to the development of steatosis by having dysregulated lipid metabolism that increases lipid production and storage while decreasing lipid breakdown.

Discussion

Understanding how cellular damage accumulates and drives degenerative diseases remains one of the most pressing challenges in biomedical research. Here, we introduce a novel strategy that quantifies cellular damage at single-cell resolution, providing a powerful tool to dissect disease progression across diverse biological systems. This integrative experimental and computational strategy leverages cell-type-specific molecular markers for the systematic stratification of cells along a damage continuum, revealing fundamental mechanisms that underlie cellular dysfunction in chronic degenerative diseases. Unlike conventional transcriptomic analyses that rely on discrete cell-state classifications, our method captures progressive molecular deterioration, offering a new paradigm to study the molecular pathogenesis of degenerative disorders.

Applying this concept to podocytes and hepatocytes, we identify conserved, damage-associated molecular programs that operate across animal models and human disease. In podocytes, we uncover a metabolic shift toward oxidative phosphorylation, likely reflecting the energy demands of cytoskeletal remodeling in response to damage. Our data further establish that focal adhesion components exhibit both universal and trigger-specific responses to injury, offering new insight into the structural adaptions of podocytes under stress. While it was already established that changes in the circadian rhythm impact podocytes[75–77], we now provide the first direct evidence that podocyte damage actively disrupts circadian gene regulation, revealing a bidirectional interplay between circadian control and podocyte health - a critical finding that underscores the role of cell-intrinsic circadian dysregulation in disease progression.

In hepatocytes, we show that progressive damage determines cellular fate, driving cells toward senescence, apoptosis, or neoplastic transformation. Notably, we identify a tipping point in hepatocyte damage beyond which metabolic capacity is irreversibly impaired, leading to the shutdown of lipid and bile acid metabolism. These findings suggest that senescent hepatocytes may serve as drivers of tissue dysfunction, potentially fueling chronic inflammation and hepatocellular carcinoma (HCC) development. The ability to pinpoint this tipping point represents a critical step toward defining therapeutic windows for intervention in liver disease progression [100].

Beyond its biological insights, our damage-scoring framework has direct clinical implications. The pathway fingerprints derived from our approach can serve as diagnostic tools for the molecular characterization of patient biopsies, enabling subtype-specific stratification of disease states. The successful application of our framework to FSGS mouse models suggests that similar damage-based signatures could be developed for clinical samples, allowing for precision medicine approaches in glomerular and hepatic pathologies. Furthermore, by performing cross-model analysis, we identify Dpp4 as a conserved hallmark of podocyte damage, suggesting that Dpp4 inhibitors - currently used in type 2 diabetes - could be repurposed for podocyte disease therapy. More broadly, this study establishes a universal blueprint for investigating degenerative diseases at a systems level, offering a scalable approach to quantify cellular damage across species and disease contexts.

The ability to apply our single-cell damage scores across *in vivo* omics modalities and cross-species datasets opens exciting new opportunities for decoding the mechanisms of chronic disease progression beyond the kidney and liver, with potential applications in neurodegeneration, fibrosis, and aging-related disorders. By shifting the focus from static disease endpoints to progressive, single-cell damage trajectories, our approach lays the foundation for a new generation of precision diagnostics and targeted therapies aimed at intercepting degenerative diseases at their earliest stages.

Material and methods

Wet lab

Animal work

Mice were housed and maintained in CECAD *in vivo* Research Facility. All mice were kept under a 12-hour light/dark cycle and had *ad libitum* access to food and water. All mouse experiments were performed with approval from the Animal Care Committee of the University of Cologne and LANUV NRW (Landesamt für Natur, Umwelt und Verbraucherschutz Nordrhein-Westfalen, State Agency for Nature, Environment and Consumer Protection North Rhine-Westphalia) for this study. All mice were kept on a C57BL6 background except for $Wt1^{ko/wt}$ mice, which were kept on an FVB/N background. $NPHS2^{mut}$ mice was published[46]. $Pdss2^{mut}$ mice were generated by the CECAD *in vivo* Research Facility. The $Wt1^{ko/wt}$ mice were previously described[101]. Mice carrying the nuclear nT-nG reporter was obtained from the Jackson Laboratory (Strain #:023035) and were

crossed to NPHS2 Cre line Pod:cre[102] to generate podocyte-specific expression of nuclear GFP (nTnG;Pod:cre).

For analysis of circadian gene expression two groups of male C57BL/6J mice aged 8 weeks and 78 weeks were acclimated for 2 weeks under 12-h/12-h light–dark cycles before euthanasia at zeitgeber times (ZT): 0, 3, …, 21 h, in accordance with the regional animal ethics committee guidelines. Duplicates of pooled samples consisting of three biological replicates were acquired per zeitgeber time and group, respectively.

Pdss2^{mut} (V117M) mice were generated as previously published[103] (Supplementary Fig. 5a).

Isolation of glomeruli and nuclei

Mice were sacrificed by cervical dislocation and kidneys were extracted and perfused *ex vivo* through the renal arteries with magnetic Dynabeads (Thermo Fisher) suspension in HBSS (5.4 mM KCl, 0.3 mM Na_2HPO_4, 0.4 mM KH_2PO_4, 4.2 mM $NaHCO_3$, 137 mM NaCl, 5.6 mM D-glucose, 1.3 mM $CaCl_2$, 0.5 mM $MgCl_2$, 0.6 mM $MgSO_4$). Perfused kidneys were minced by scalpel and digested with digestion buffer (1 mg/ml Pronase E (Sigma), 1 mg/ml collagenase type II (Worthington) and 50 U/ml Dnase I (Applichem) in HBSS) for 15 minutes at 37 ℃. The kidney suspension was triturated until homogenous and filtered twice through 100 µm cell strainers. The kidney lysates were washed with HBSS and pelleted at 1500 rpm for 5 minutes at 4 ℃. The pellet was resuspended in HBSS and washed on the magnet until isolated glomeruli were obtained.

Isolated glomeruli were resuspended in 1 ml of lysis buffer (EZ lysis buffer (Sigma) supplemented with EDTA-free protease inhibitors (Roche)) and shaken at 1400 rpm for 10 minutes at 4 ℃. After magnetization, the supernatant containing loose nuclei was collected through a 30 µm cell strainer. The leftover beads were resuspended in 1 ml lysis buffer further lysed 5 times through a 27-G needle. After the loose nuclei were collected, the beads were resuspended in 1 ml of lysis buffer and further lysed through a 30-G needle 5 or 10 times to collect the final aliquots of loose glomerular nuclei. The pooled nuclei were centrifuged at 500 g for 5 minutes at 4 ℃. The pellet was resuspended in 300 µl of lysis buffer, transferred to a 1.5 ml tube and placed on the magnet for 3 minutes to remove residual magnetic beads.

ATAC-seq

50,000 nuclei were isolated from nTnG;Pod:cre isolated glomeruli, stained with DAPI (Thermo Fisher) and sorted using the FACSAria III (BD) equipped with the 70 µm nozzle with chillers. Singlet and DAPI+ nuclei were gated by forward scatter and side scatter and the UV1 laser. DAPI+ nuclei were then sorted by fluorescent signal and collected into EZ lysis buffer (Sigma)

supplemented with protease inhibitors (Roche). Nuclei were centrifuged at 1000 g for 10 minutes at 4 ℃ and resuspended in 50 µl of transposition reaction mix (25 µl of transposition buffer, 2.5 µl of TDE1 (Illumina) and 22.5 µl of nuclease-free water). The reaction was carried out at 37 ℃ for 30 minutes. Immediately following transposition, DNA was purified using the DNA clean concentrator-5 kit (Zymo) per manufacturer's instructions. Library preparation and sequencing were performed by the Cologne Centre of Genomics (CCG).

Single nuclei RNA-seq

Glomeruli were isolated from murine kidneys and subjected to isolation of nuclei using EZ lysis buffer (Sigma) supplemented with 0.1% murine RNase inhibitor (NEB). Isolated nuclei were counted with a hemocytometer. After centrifugation at 1000 g for 10 minutes, nuclei were resuspended in PBS supplemented with 2% BSA (Carl Roth) to reach an approximate concentration of 1000 nuclei per µl. Prior to immediate processing, the samples were further filtered through a 10 µm strainer. For $Wt1^{ko/wt}$ and $Nphs2^{mut}$ mice, glomeruli nuclei were used for snRNA-seq. For $Pdss2^{mut}$ mice, glomeruli nuclei were combined with nuclei extracted from whole kidney (1:1 volume) to additionally capture tubules. Libraries and sequencings were prepared per the manufacturer's instructions supported by 10X Genomics.

Bulk RNA-seq

For analysis of circadian gene expression in kidneys, whole kidneys were dissected, snap-frozen and RNA was prepared using the miRNeasy mini Kit (Qiagen) to isolate total RNA. After removal of ribosomal RNA using biotinylated target-specific oligos combined with Ribo-Zero ribosomal RNA removal beads, RNA was fragmented into small pieces and copied into first-strand complementary DNA (cDNA) followed by second-strand cDNA synthesis. Products were purified and enriched with PCR to create the final cDNA library. After library validation and quantification (2100 Bioanalyzer; Agilent), equimolar amounts of five to six pooled libraries were quantified by using the Peqlab KAPA Library Quantification Kit and the Applied Biosystems 7900HT Sequence Detection System and sequenced on a Hiseq2000 sequencer.

STED Microscopy

Kidney tissues were fixed in formalin overnight at 4 ℃ and stored in PBS. Kidney cortex was cut into 1-2 mm pieces and immersed in hydrogel solution (4 % acrylamide (Carl Roth), 0.25 % VA-044 initiator (Sigma) in PBS) overnight at 4 ℃. The gel was polymerized by incubation at 50 ℃

for 3 hours. Excess polymer was removed and tissues were washed in PBS three times and embedded in 3% agarose (Carl Roth) prior to cutting into 200 µm sections with a vibratome (Leica). Samples were transferred to a clearing solution (200 mM boric acid, 4 % SDS, pH 8.5) and incubated at 50 ℃ until cleared. Samples were washed briefly in a wash buffer (10 mM HEPES, 200 mM NaCl, 3 % Triton X-100) before incubation with primary antibodies (nephrin: 20R-NP002, Fitzgerald; THSD7A: HPA000923, Sigma; claudin-5: 35-2500, Thermo Fisher) at 1:100 at 37 ℃ overnight. Samples were washed with wash buffer before incubation with secondary antibodies (anti-guinea pig: 106-005-003, Jackson ImmunoResearch; anti-rabbit: 711-005-152, Jackson ImmunoResearch; anti-mouse: 115-005-003, Jackson ImmunoResearch; each conjugated to fluorophores in-house) at 1:100 at 37 ℃ overnight and embedded in saturated fructose solution (80.2 % w/w fructose, 0.5 % α-thioglycerol (Sigma)) before mounting in a glass-bottom dish (Ibidi) for imaging with the SP8 STED microscope (Leica).

Data Analysis

Statistical data analysis and visualization was performed in the R programming environment.

Raw data analysis

Data retrieval and quality control

Raw sequencing files of published datasets available in the 'sra' format were extracted and converted to 'FASTQ' format using the SRA Toolkit (version 2.11.3). Quality control of FASTQ files was done with FastQC version v0.11.9[104] MultiQC version v1.1[105] was used to summarize the quality statistics of multiple samples from one study into a comprehensive overview. No samples were excluded due to lack of quality.

RNAseq

An index of the *Mus musculus GRCm38 (mm10) and* GRCm39 reference genomes and its annotations were generated using STAR v2.7.3[106] aligner to be used for alignment of raw reads from liver and kidney studies, correspondingly. When STAR was run to align reads, the option -quantMode' was set to the command 'GeneCounts' to generate count matrices as an output. Gene abundances were quantified using both exonic and intronic reads with pre-mRNA full gene models.

STARsolo function of the STAR aligner was used to map reads of single nuclei RNAseq experiments. Sequence files from 2 sequencing lanes, if present, were pulled in one sample. Ambient RNA was removed from UMI count tables using decontX v1.2.0 R package[107].

The read count (UMI) matrices of all single cell RNAseq samples were processed in Seurat v4.0.1 R package[108], cells with less than 500 features and genes expressed in less than 100 cells were filtered out. Cells with more than 1% of mitochondrial RNA were also discarded.

ATACseq

Mapping to the mouse genome mm10 was done using bwa mem 0.7.17 with default parameters. Data quality was assessed by calculating the insert sizes between the R1 and R2 read pairs. Peaks were called using Genrich v0.6.1 tool, provided as an open-source software package available at GitHub (https://github.com/jsh58/Genrich#quick).

Spatial transcriptomics data analysis

Mouse kidney spatial transcriptomics

Kidney Slide-seq V2 spatial transcriptomics data was taken from GSE190094[45]. Podocyte annotation and KNN filtration, glomerular identification and size estimation was performed using the original code from the publication[45]. Samples with low capture rates (below the average of 100 features per bead) and without visually detectable podocyte clusters were removed, excluding 20 out of 49 original samples from the downstream analysis. For the remaining 29 samples the number of beads annotated as podocytes was normalized to the glomerular area and subsequently the bead density per glomerulus was correlated with the average PDS of the respective glomerulus.

Mouse liver spatial transcriptomics

HDS was applied on spatial transcriptomic data from the Liver Cell Atlas data set[9]. Seurat was used to analyze the 10X Visium counts. After exploratory analysis, uninformative spots that were in regions with no or minimal tissue were removed. Filtering for sequencing quality control was performed with same parameters as in the ‘Liver Cell Atlas Git Hub’. Spots were kept that had more than 1000 features detected (‘nFeature’) and a total number of counts (nCount) higher than 5000 and lower than 60 000, as well as not more than 15% mitochondrial RNA. Then we calculated the HDS per spot as detailed below

Human kidney spatial transcriptomics

We used KPMP 10X Visium spatial transcriptomic data from a human with FSGS, patient ID 29-10282. The count data and the spots coordinates were loaded and processed with Seurat v4.0.1[108]. Glomeruli were annotated manually. The PDS was calculated for all spots annotated as glomeruli as detailed below.

Proteomic data analysis

The dataset PXD016238[13] containing proteomic data of endothelial cells, podocytes, and mesangial cells from healthy mouse kidneys was analyzed to check cell-type specific protein levels of the 42 podocyte damage markers. The LFQ data was processed with the DEP v1.4.1[109]. Only proteins expressed in more than 50% of the replicates of at least one condition were considered.

Collection of kidney and liver disease model expression data

CEL files were downloaded for microarray data. UMI count tables were downloaded for single cell RNA-seq experiments. Unnormalized gene expression count matrices were used, when available, in case of bulk RNA sequencing experiments. If the data was not available in this format, unnormalized count matrices were generated from raw reads, as described above.

Gene IDs were mapped to Mouse Genome Informatics (MGI) gene symbols as a common reference using the R package 'biomaRt' version 2.50.2[110,111]. On a few occasions, if the expression data set included counts for different splice variants of the same gene, the average expression across the splice variants was taken as the expression count of that gene before converting to MGI nomenclature, since MGI nomenclature does not account for alternative splicing.

Differential gene expression analysis

CEL files for microarray data were processed and differential expression analysis performed using the oligo v1.54.1 R package[112] with the default parameters. Non-normalized bulk RNAseq count tables were subjected to differential expression analysis with DEseq2[97] v1.34.0 with the default parameters. For hepatocyte data, counts were transformed using the variance stabilizing transformation in DESeq2 with the parameter 'blind' set to 'true'. Single cell RNAseq UMI count tables were processed and differential expression analysis performed with Seurat v4.0.1[108] using the FindMarkers() function with the default parameters. In case of the single cell data only cells

of the respective cell type were considered (i.e. podocytes or hepatocytes). Gene set over-representation analysis was done using ClusterProfiler, version 4.10.1[113].

Candidate gene lists for PDS and HDS marker genes

Candidate lists for damage markers were generated to ensure that marker genes were expressed in the targeted cell type (here: podocyte for PDS, hepatocyte for HDS). Data from diseased and control samples was included. The expression of genes included in damage scores was not required to be exclusive to the targeted cell type, allowing for the inclusion of marker genes that are generically expressed in various cell types.

To create a catalogue of genes expressed in podocytes we used three single-nuclei RNAseq kidney datasets generated within this study, and four published single-cell RNAseq kidney datasets from GSE146912[55] (Supplementary Table 1), each of the datasets representing a unique podocyte damage model. Cells annotated as podocytes were subset from all 7 datasets and used for the selection.

To create a catalogue of genes expressed in hepatocytes we used murine gene expression data from the Liver Cell Atlas (https://livercellatlas.org/download.php). All the following steps were carried out using the R package Seurat[114]. Cells annotated as hepatocytes by the authors were subset from the two experiments available: Standard Diet and Non-Alcoholic-Fatty-Liver-Disease (NAFLD).

The selection procedure for identification of genes expressed in podocytes and hepatocytes single-cell RNAseq data was identical. A detection rate for each gene was calculated across cells that fulfilled the following criteria: ‘nFeature_RNA’ greater than 500 and lower or equal to 6,000, less or equal to 2.5 % mitochondrial RNA and ‘nCount_RNA’ smaller than 30,000. Genes with a detection rate of at least 0.03 (i.e. 3% of the cells) in the target cell type were kept for the subsequent analyses.

Damage score

Damage score algorithm

To generate the damage scores, we selected and analyzed datasets that represent different disease models and that were partially obtained using different experimental platforms (Supplementary Table 1). Novel data was generated for the PDS (see above and Supplementary

Table 1). First, each dataset was individually processed and analyzed to obtain differentially expressed genes, always comparing experimental condition versus control. In case of the single cell data only cells of the respective cell type were considered (i.e. podocytes or hepatocytes). Results of differential expression analysis were integrated across studies in the following way:

1. Gene must be identified as potentially expressed in podocytes or hepatocytes respectively.
2. Genes were selected if they were detected in >=75% of the studies.
3. Out of those, genes were kept if their fold changes were in the same direction (i.e. either positive or negative fold change) in >=75% of the studies.
4. Selected genes were ranked by their p-value of differential expression per study. P-values for differential expression may not be comparable between studies, due to variation in sample numbers and/or variable quality of the data. We therefore decided to base the selection process on ranks of p-values rather than defining a common p-value threshold across studies.
5. Ranks were combined across studies by averaging the rank of each gene.
6. Genes were sorted by their mean rank, and the top N (N = 42 for the final score) were selected as a universal damage signature. In the calculation of the score, damage signature genes were treated differently depending on whether they were up or downregulated under the disease condition (see below).

Damage scores were computed for each cell/spot/sample using the damage signature genes with the AUCell[12] R package. AUCell scores were calculated separately for up and down regulated genes and combined as follows to get the final podocyte damage score:

$$DS = \frac{n_{up}}{42} DS_{up} - \frac{n_{down}}{42} DS_{down}$$

where DS_{up} and DS_{down} are the respective AUCell scores obtained with the up and downregulated genes. Note that the AUCell score is negative for low-ranking genes. These scores were weighted based on the number of up and down regulated genes (n_{up}, n_{down}). Since in both cases (PDS and HDS) the majority of genes were downregulated, DS_{down} contributed more to the final damage score DS.

Damage score validation

Leave-one-model-out cross-validation

Cross validation was performed by excluding all data of one disease model group (Supplementary Table 1) from the training procedure. Damage signature genes were determined as described above on the remaining training data. Subsequently, damage scores were computed as described above on the samples from disease model left-out for testing.

Damage signature size test

The effect of damage signature size on damage score performance was evaluated by scoring sc/snRNA-seq studies with sets of the top 5, 10, 15, 20, 30, 40, 50, 100, and 200 genes of the PDS damage signature, respectively.

Damage signature randomization test

Robustness of the PDS was tested by randomizing an increasing percentage of studies used to generate the PDS by means of shuffling p-values and LFCs of differential expression results. Signatures for partially randomized data were generated and used to calculate deviant damage scores in a snRNA-seq dataset. As the choice of studies for randomization likely affects the resulting scores, 50 rounds of subsampling of studies were carried out for each level of randomness (i.e. percentage of randomized studies) and results were averaged separately for control and experimental conditions of the test dataset (nephrotoxic serum nephritis, GSE146912[55]).

Damage signature transfer to human data

Damage signature genes in humans were determined by manually mapping mouse genes to their human orthologs using the MGI gene annotation[115]. Signature genes without known human orthologs were omitted. In cases of several human orthologs to a single mouse gene, we kept all human orthologs. In cases of several mouse disease signature genes with a single human ortholog, we included the human ortholog and reduced the number of genes contributing to score calculation.

Pseudo-time trajectory inference

After filtering hepatocytes based on annotation and quality control metrics using Seurat, we performed psuedo-time trajectory (PT) inference on normalized counts of each sample separately. We used TSCAN[54], because it allows for ordering cells based on the dimension

reduction results obtained in previous analyses (i.e. the principal components of the PCA) and does not need prior knowledge.

Pathway activity analysis

Pathway activity was defined as the AUCell v.1.12.0 score[12] obtained for the set of genes annotated as pathway members. Pathway membership (i.e. gene annotation) was taken from Reactome, KEGG and 50 hallmarks from MSigDB[116]. This scheme was used to compute relative pathway activities per single cell and for bulk RNA-seq samples. To obtain pathway signatures of the damage models we computed Spearman correlation of single-cell pathway activities with the PDS for each damage model and for the cumulated controls. Per disease model, the top 10 significantly correlating pathways were included in further analyses (adjusted p-value < 0.05), resulting in a set of 85 pathways. Of those 85 pathways, 26 pathways were manually selected for visualization in Fig. 3a.

Transcription regulatory network construction

To identify transcription factors (TFs) expressed in podocytes, we utilized sc/snRNA-seq data from podocytes as follows: we selected TFs with a detection rate above 5% in at least one of the analyzed sc/snRNA-seq datasets, which resulted in 110 Transcription factors that were used to construct the podocyte transcription regulatory network (TRN). A TRN is a directed graph representing interactions between transcription factors and their target genes. The TRN was constructed using the podocyte ATAC-seq data and known transcription factor binding motifs in following steps:

ATAC-seq footprinting was performed on the ATAC-seq peaks with TOBIAS v0.14.0 to more precisely locate putative TF binding events[117].

Motif scanning was done on ATAC-seq footprints using FIMO from the MEME-suit v5.5.0[118]. Motif hits with a p-value < 5e-4 were kept for the analysis.

Motif hits (i.e. potential TF binding sites) for each of the 110 TFs were associated with putative target genes using the ClosestGene approach implemented in the TFtargetCaller v0.7 R package[119]. Genes with a q-value < 0.1 were assigned as targets of the corresponding TF.

TFs of a common family often have very similar or even identical position weight matrices (PWMs) resulting in virtually identical DNA binding motif predictions. To address this ambiguity, PWMs of 110 analyzed TFs were subjected to hierarchical clustering, resulting in 14 TF motif clusters with

high similarity of motif sequences and predicted target genes within each TF family. We combined predicted targets of all TFs within each family into one regulon for the downstream analysis.

Circadian clock analysis

Identification of kidney specific circadian genes

Bulk RNAseq data from kidneys of young (10 weeks) and old (80 weeks) mice were used to identify kidney-specific circadian genes. Cycling genes were identified with the meta2d(cycMethod = “"JT”") function from MetaCycle v1.2.0[120]. Overall, 317 genes with BH adjusted p-value <0.01 in either young or old mice were called ‘circadian’. Estimation of acrophase and acrophase uncertainty for circadian genes was done by fitting a cosinor model with the cglmm(Y ~ amp_acro(time_col=Time, period = 24)) function of GLMMcosinor v0.2.0.9 R package, where Y are the rlog-normalized expression values of a gene.

Circadian rhythm disruption

Circadian rhythm disruption (CRD) in individual podocytes was calculated using cal_CRDscore() from the CRDscore v0.1.0 R package[79]. The set of cycling genes identified from the kidney circadian bulk RNAseq was used to calculate CRD. The open-source CRDscore R package is provided at GitHub: https://github.com/yixianfan/CRDscore.

Tempo

Circadian time in individual podocytes was estimated by the Tempo algorithm[78] using expression of core clock genes. Estimates of gene acrophases, required by the algorithm, were taken from the analysis of bulk circadian RNAseq data from the mouse kidney dataset. Clock was used as the reference gene.

Tempo is provided as an open-source software package available at GitHub https://github.com/bauerbach95/tempo .

Hepatocyte cell fate analysis

We used AUCell to calculate the activity score of genes in the SenMayo gene set, that was developed to identify senescent cells[81]. We then used the HDS and SenMayo activity scores to classify the hepatocytes into five cell fate trajectories. We considered the HDS distribution across all samples (global distribution) to set undamaged/damaged hepatocyte thresholds, and used the

SenMayo activity score distribution of the most damaged samples (9-month-old NASH) to set a senescent cell fate threshold. Thus, we considered a hepatocyte undamaged if its HDS was smaller than the global 25%-quantile. Hepatocytes with an HDS between the global 25%- and 75%-quantile were considered hepatocytes in “transition” to a damage state. We divided the damaged hepatocytes (with HDS over the global 75% quantile) into the cell fate trajectories “senescent”, “unresolved” and “not senescent”. Senescent-like hepatocytes had a SenMayo activity score over the 75%-quantile of the 9-month-old NASH distribution, while not-senescent like cells had a value under the 25%-quantile. Damaged hepatocytes with a SenMayo activity score in between these upper and lower thresholds were considered to be in “damaged unresolved” cell fate.

To find genes differentially expressed in damaged senescent hepatocytes when compared to not-senescent damaged hepatocytes, we used Seurat’s FindMarkers function on a SC-transformed merged Seurat object. By default, the function utilizes a Wilcoxon Rank Sum Test. FindMarkers performs p-value adjustment using Bonferroni correction based on the total number of genes expressed. We considered genes significantly differentially expressed if they had an adjusted p-value < 0.05, an absolute Log2 fold change > 0.5 and were expressed in at least 10 % of hepatocytes of either senescent-damaged or not-senescent damaged clusters.

Resource availability

Data availability

All sequencing data generated within the study has been made available at Gene Expression Omnibus (GEO) under the accession number GSE289878.

Code availability

All code has been made available on GitHub at:

https://github.com/beyergroup/PodocyteDamageScore

https://github.com/beyergroup/HepatocyteDamageScore

Declaration of interests

The authors declare no competing interests. All funding sources are listed in the Acknowledgements section.

Acknowledgements

We thank C. Schell for valuable discussions and providing protein interaction networks. The Wt1 knock-out mouse was a gift from Jordan A. Kreidberg. We thank the FACS & Imaging Core Facility at the Max Planck Institute for Biology of Ageing, Cologne and the CECAD Imaging Facility, Cologne for their support in FACS and imaging acquisition, respectively. We thank S. Lück, P. Thaben, and A. Kramer for assistance with circadian bulk RNA-seq mouse experiments. H.C. and P.U.A. received support from the Cologne Graduate School of Ageing Research. This study was conducted within CRU329 at the University of Cologne and was supported by grants from the German Research foundation (BE2603/10-1, BE2603/10-2 to A.B.; KA3217/5-1, KA3217/5-2, KA3217/6-1 to M.K.; MU3629/4-1 to R.U.M; BR6668/2-1 to F.B.). The work was supported by German Ministry for Education and Research grants 0315899 (to P.O.W.) and 01EO2106 (to F.B.).

Author Contributions

T. P., P. U. A., and H. C. contributed equally to this work. M. K. and A. B. jointly supervised the project. T. P., P. U. A., H. C., M. K., and A. B. conceptualized the study. T. P. and P. U. A. performed computational analyses. H. C. carried out experiments. F. B., P. W., and R. U. M. generated data for circadian rhythm analyses. C. Ö., P. T. B., and B. S. generated mouse models. T. P., P. U. A., H. C., M. K., and A. B. generated figures. F. T. W. provided expertise on liver biology, T. B. provided expertise on podocyte biology. T. P., P. U. A., H. C., T. B., M. K., and A. B. wrote the manuscript. All authors approved of the manuscript.

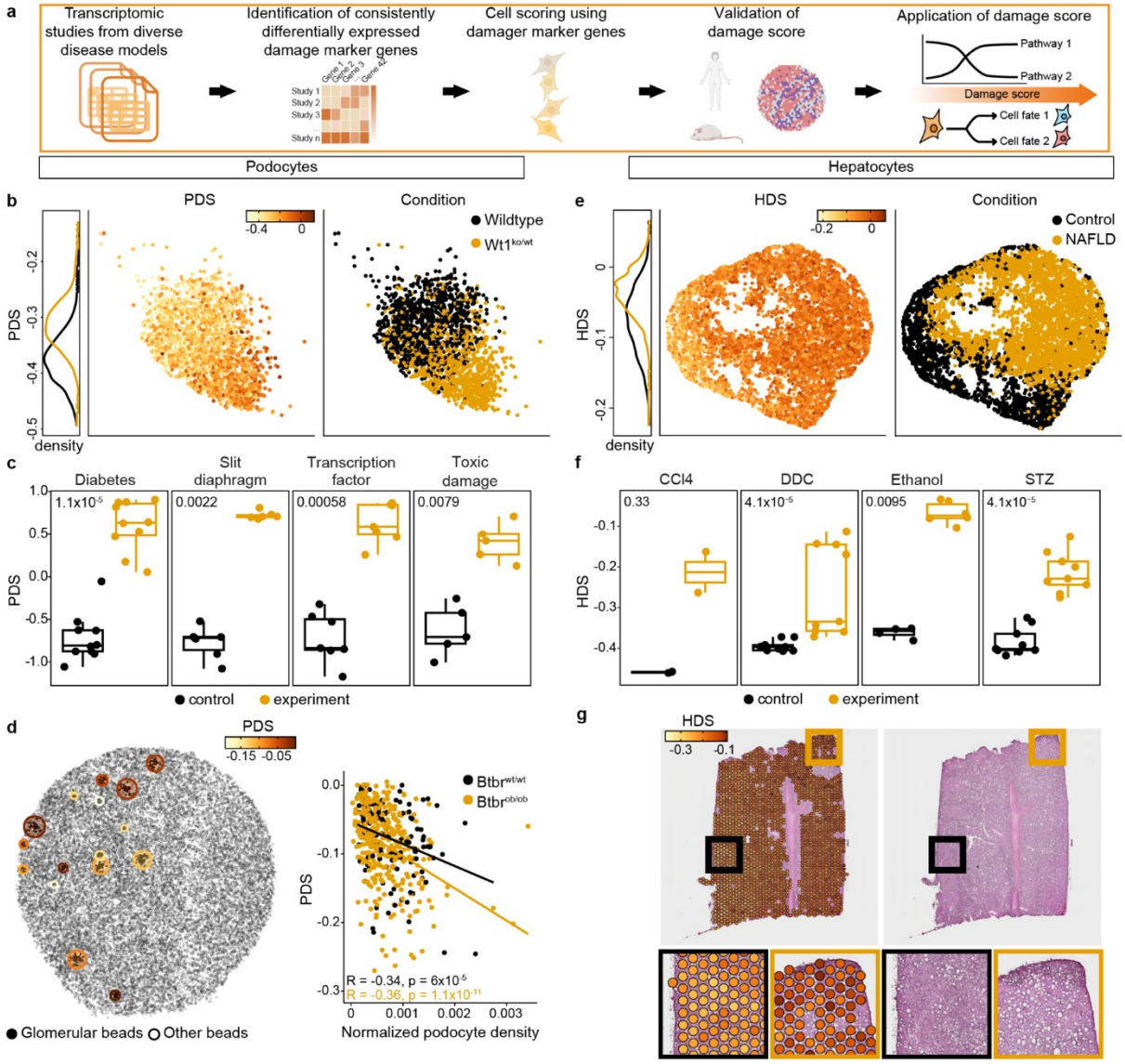

Figure 1: A strategy to quantify damage at the single cell level based on transcriptomic data.

a. Robust damage marker genes are identified by compiling transcriptomic data from a great diversity of disease models. Top genes that change consistently across models are selected as damage markers. Damage of individual cells is quantified using a rank-based approach. After validation, the damage scores are used to analyze the molecular progression of chronic degenerative diseases *in vivo*.
b. Application of the podocyte damage score (PDS) to podocytes from snRNA-seq data of the $Wt1^{ko/wt}$ mouse model (a podocyte damage model). Left UMAP is colored by PDS (see color scale), right UMAP is colored by condition. The PDS density plot (left) shows the distribution of PDS values separated by experimental condition (same colors as UMAP on the right).
c. Leave-one-model-out cross validation of the PDS. All data of the indicated disease models were left out during the creation of a variant damage signature and used afterwards for testing PDS in the indicated disease models (see Supplementary Table 1 for grouping). Each dot represents the average damage score per sample, scores are scaled and centered per study. P-values of Wilcoxon rank test (experimental versus control conditions) are shown. The boxplots show first (Q1), second, and third quartiles (Q) of distribution. Whiskers represent Q1 - 1.5 x interquartile range (IQR) and Q3 + 1.5xIQR.Spatial validation of the PDS using kidney Slide-seqV2 spatial transcriptomics data on diabetic $Btbr^{ob/ob}$ and control kidneys (GSE190094[45]). Representative section of a diabetic mouse kidney is

shown. Circles represent glomerular areas and are colored by the mean PDS calculated for podocyte beads (as determined in [45]) within one glomerulus. The PDS correlated with glomerular size (higher PDS for larger glomeruli), albeit without correction for tissue sectioning-related artifacts. Right plot shows PDS measurements normalized for podocyte density after correcting for area variance caused by tissue sectioning and reveals increased podocyte damage corresponding to hyperfiltration in low podocyte density settings such as diabetes or large glomeruli (see Supplementary Fig. 3b for density calculation).

d. Application of the hepatocyte damage score (HDS) to hepatocytes of snRNA-seq data from 24-week-old mice fed with either a standard diet (control) or a NAFLD-inducing diet (NAFLD)[9,48]. Left UMAP is colored by HDS (see color scale), right UMAP is colored by diet. HDS density plot (left) shows the distribution of HDS values separated by experimental condition (same colors as UMAP on the right).
e. Leave-one-model-out cross validation of the HDS. Procedure is the same as in c. Each dot represents the HDS of one sample. CCl4: hepatic toxic injury by CCl4 injection, DDC: hepatotoxin-induced cholestatic liver injury via 3,5-diethoxycarbonyl-1,4-dihydrocollidine, Ethanol: alcoholic liver injury via ethanol administration, STZ: streptozotocin induced liver injury. Boxplots show first (Q1), second, and third quartiles (Q) of distribution. Whiskers represent Q1 - 1.5 × IQR and Q3 + 1.5 × IQR. P-values of Wilcoxon rank test (experimental versus control conditions) are shown.
f. Spatial validation of HDS using 10X Visium mouse spatial transcriptomic data[9,48]. Liver tissue section of a mouse with NAFLD. Left: HDS computed for each spot that passed filtering in spatial transcriptomics data. Right: Corresponding H&E staining. Indicated areas are enlarged as insets, in which HDS correlates with the degree of lipid accumulation. For additional data see Supplementary Fig. 3d.

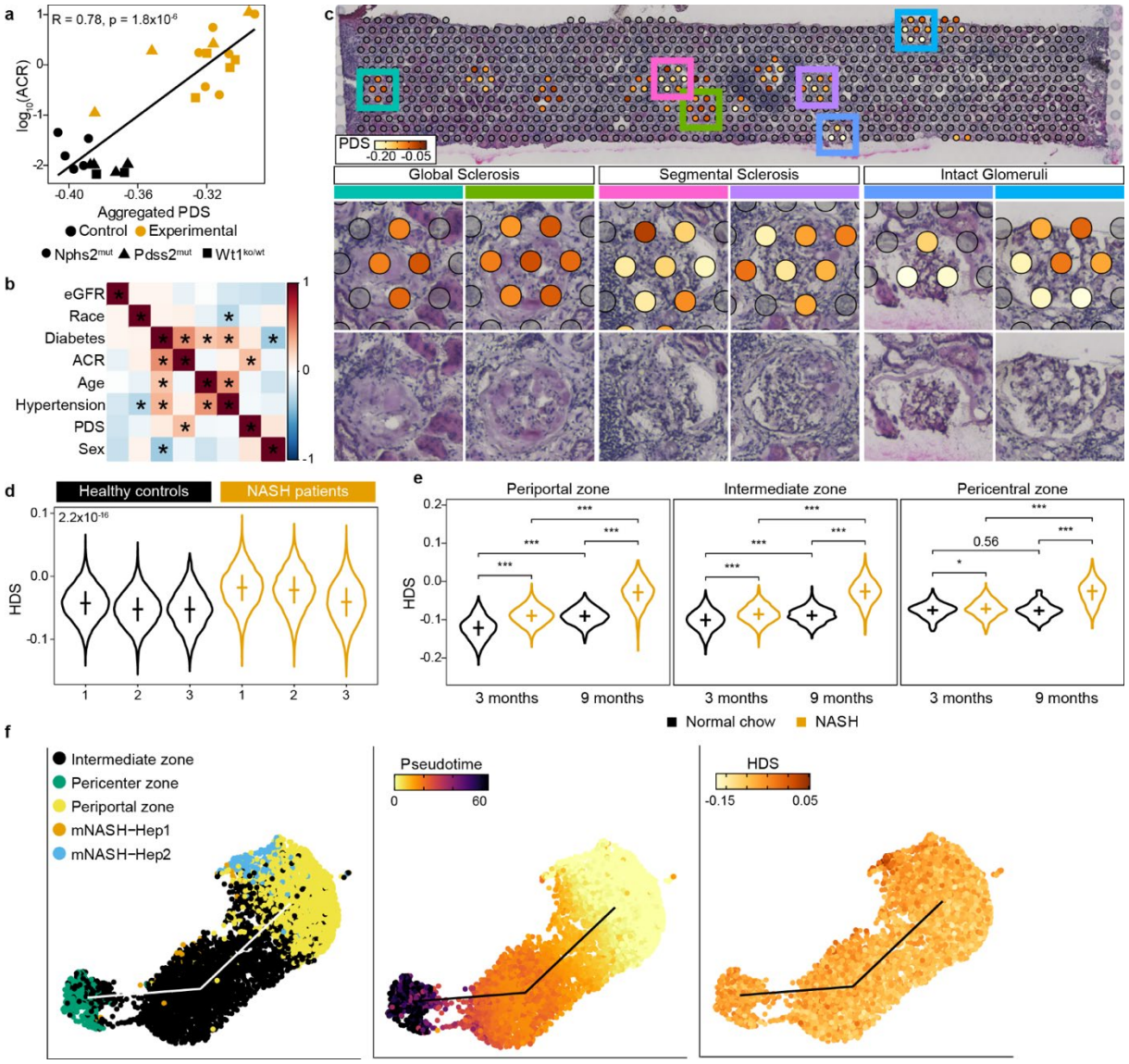

Figure 2: Functional validation of PDS and HDS on mouse and human datasets

Kidney

a. Correlation between albuminuria (logarithm of the Albumin/Creatinine ratio in mg/mg (ACR)), an established clinical measure of podocyte damage, and the PDS for three different murine disease models (Nphs2^{mut}, Pdss2^{mut}, Wt1$^{ko/wt}$). Cells of each snRNA-seq sample were aggregated ('pseudo-bulk'). Shape and color represent the study and experimental status of the sample, respectively.
b. Spearman rank correlation between the PDS and clinical attributes of acute kidney injury (AKI) and chronic kidney disease (CKD) patients as provided in the KPMP kidney tissue atlas (https://atlas.kpmp.org/). Asterisks denote correlations with P-value < 0.05. scRNA-seq (N=17) and snRNA-seq (N=37) data from patients with available albuminuria measurements were used. (eGFR: estimated glomerular filtration rate; ACR: urinary albumin/creatinine ratio)
c. 10x Visium spatial transcriptomic data on a human kidney biopsy from the KPMP registry (patient ID 29-10282[3]) showing an FSGS phenotype. PDS values were computed only for Visium spots with podocyte signals as determined by Wt1 and Nphs2 expression. Selected glomeruli are marked in the upper panel with respective colors. High magnification images show various degrees of glomerular sclerosis with PDS gradients corresponding to degree of sclerosis. See boxplots for PDS distribution as by glomerular damage in Supplementary Fig. 4c.

Liver

d. HDS marker genes were mapped to human ortholog genes to test the transferability of the score trained on mouse data to human data. The distributions of HDS calculated on human hepatocyte snRNA-seq data from three healthy donors and three individuals with NASH (GSE189600[52] are shown). Age and sex of healthy donors: 47 y/o female, 50 y/o male and 50 y/o male. Age and sex of NASH patients: 49 y/o male, 64 y/o female and 31 y/o male. Horizontal lines show median of the distribution and vertical lines represent the IQR. P-value of Wilcoxon rank test (NASH versus healthy) is shown.

e. HDS in relationship to liver zonation; data taken from (GSE189600[52]). Male mice were fed with standard or NASH promoting diet at 4 weeks of age for 3 or 9 months (n = 1). HDS distributions for cells from control (black) and NASH inducing diet (orange) are shown. Horizontal lines show median of the distribution and vertical lines represent the IQR. P-values from Wilcoxon rank sum test are shown and * < 0.05, ** < 0.01, *** < 0.001. Hepatocyte zone annotation provided by authors of data set (GSE189600[52])

f. HDS versus pseudo-time trajectories (PT), same data as in e; UMAPs show hepatocytes of a 9-month-old mouse fed NASH inducing diet. Each dot represents a hepatocyte colored by liver zone (left), PT (middle) and HDS (right). Hepatocyte zone annotation from original publication[52]. MNASH-Hep1/2: classification from original publication corresponding to damaged hepatocytes whose zone of origin could not be determined according to the authors. PT correlates with zonation, while the HDS is independent of liver zonation. See Supplementary Fig. 4f for additional data.

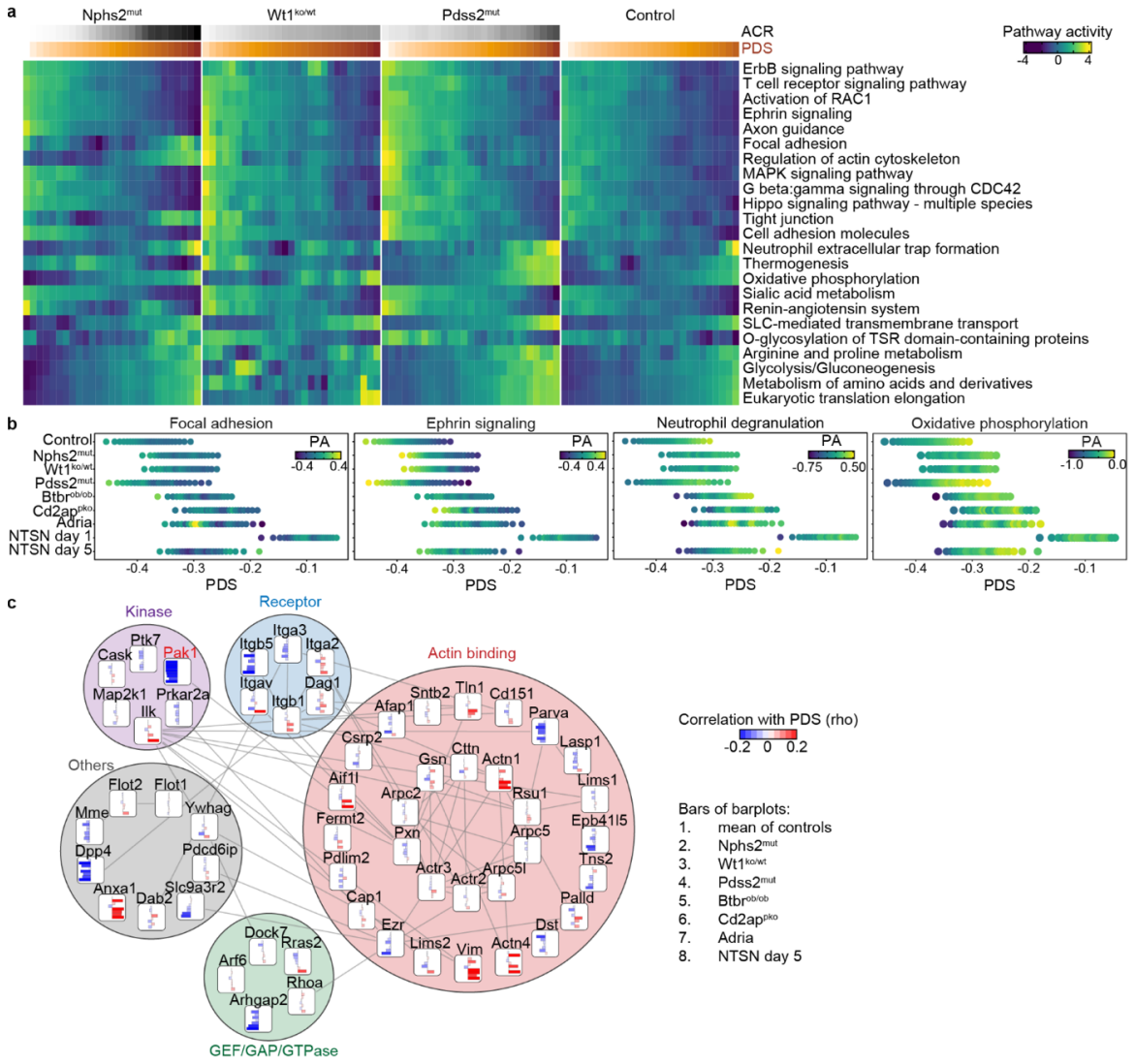

Figure 3: Application of PDS to FSGS datasets reveals model-specific pathway fingerprints

a. PDS pathway fingerprints for single-nucleus RNAseq data from Nphs2^{mut}, Wt1$^{ko/wt}$ and Pdss2^{mut} models of FSGS. 'Control' is the average of control samples from all three studies. Nuclei were sorted by increasing PDS (color bar on top). Pathway activities for KEGG and Reactome pathways were calculated using AUCell (see Methods) and smoothed using a sliding window of width twice bigger than step size, both adjusted to produce 27 bins in each study. Color shows pathway activities centered and scaled per pathway. Activity of pathways shown is significantly correlated with PDS in at least one of the three studies (Spearman rank correlation; adj. P-value < 0.05). Rows are clustered by pathway similarity. Rows on top show average albumin/creatinine ratio (ACR) and the average PDS per bin.

b. Pathway activities for selected pathways calculated on sn/scRNA-seq data of cumulated control samples and various disease models. Cells/nuclei were grouped in evenly sized bins of 30 cells/nuclei with similar PDS (x-axis). Color indicates pathway activity (PA) centered and scaled per pathway. 'Control' corresponds to the average pathway activities across control cells of all models. Range of PDS per model reflects different damage levels between models and cumulated controls.

c. Integration of a focal adhesion protein-protein interaction network[62] with PDS analysis. Bars inside each node show Spearman rank correlation (rho, see color scale) between PDS and the expression level of the gene per disease model (see legend on the right). Red and blue colors depict positive and negative correlations, respectively. Saturation of the color and length of the bar reflect strength of correlation. The marked upregulation of Actn1, Anxa1, and Vim exclusively in studies applying scRNA-seq with prior glomerular digestion is likely a technical artifact. Pak1 (marked in red) is a PDS marker gene.

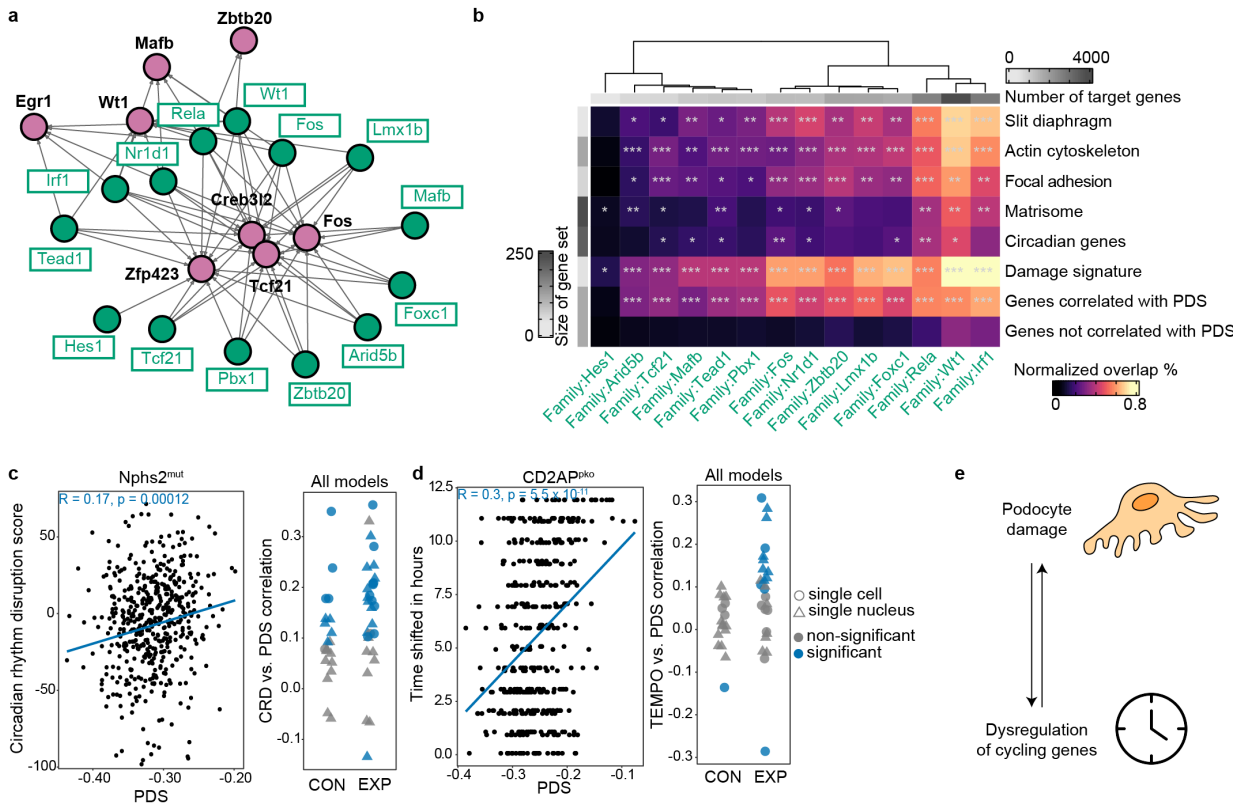

Figure 4: PDS reveals mechanisms of FSGS

a. Podocyte transcriptional regulatory network (TRN), limited to transcription factor (TF) genes correlating with PDS in multiple studies (magenta nodes) and TF family regulons (green nodes). Edges indicate regulation of TF gene by respective TF family.

b. Overlap of TF target genes with selected gene sets. Color intensity shows the fraction of genes in gene sets (rows) regulated by the respective TF families (columns). Significance of the overlap was calculated with Fisher's exact test, FDR-adjusted, and depicted on the heatmap with asterisks: *** $q < 0.001$, ** $q < 0.01$, * $q < 0.1$. Row and column annotation bars reflect size of gene sets, darker color means greater gene set. Bottom row: TF target enrichment for 100 randomly selected genes that are expressed in podocytes, but do not correlate with the PDS as a negative control.

c. Left: Relationship of circadian rhythm disruption (CRD) score[79] and PDS. Each dot represents one single nucleus from snRNAseq data of podocytes isolated from one individual $Nphs2^{mut}$ mouse. Regression line and parameters for Spearman rank correlation are shown. Right: Spearman rank correlation coefficients (calculation as exemplified for one individual mouse on the left) for all individual control (CON) and experimental (EXP) samples of seven different mouse models of podocyte damage ($Nphs2^{mut}$, $Pdss2^{mut}$, $Wt1^{ko/wt}$, $Btbr^{ob/ob}$, NTN day 5, $Cd2ap^{pko}$, Adria). Color distinguishes if the CRD-PDS correlation was significant ($p < 0.05$).

d. Left: Relationship of absolute deviation of estimated circadian time from the reference sample time and the PDS. Circadian time of each cell was estimated by the TEMPO algorithm, using Clock as the reference gene. Each dot represents one cell from scRNA-seq data of podocytes isolated from one individual $Cd2ap^{pko}$ mouse. Regression line and parameters for Spearman rank correlation are shown. Right: Spearman rank correlation coefficients (calculation as exemplified for one individual mouse on the left) for all individual control (CON) and experimental (EXP) samples of seven different mouse models of podocyte damage ($Nphs2^{mut}$, $Pdss2^{mut}$, $Wt1^{ko/wt}$, $Btbr^{ob/ob}$, NTN day 5, $Cd2ap^{pko}$, Adria). Color distinguishes if the TEMPO to PDS correlation was significant ($p < 0.05$).

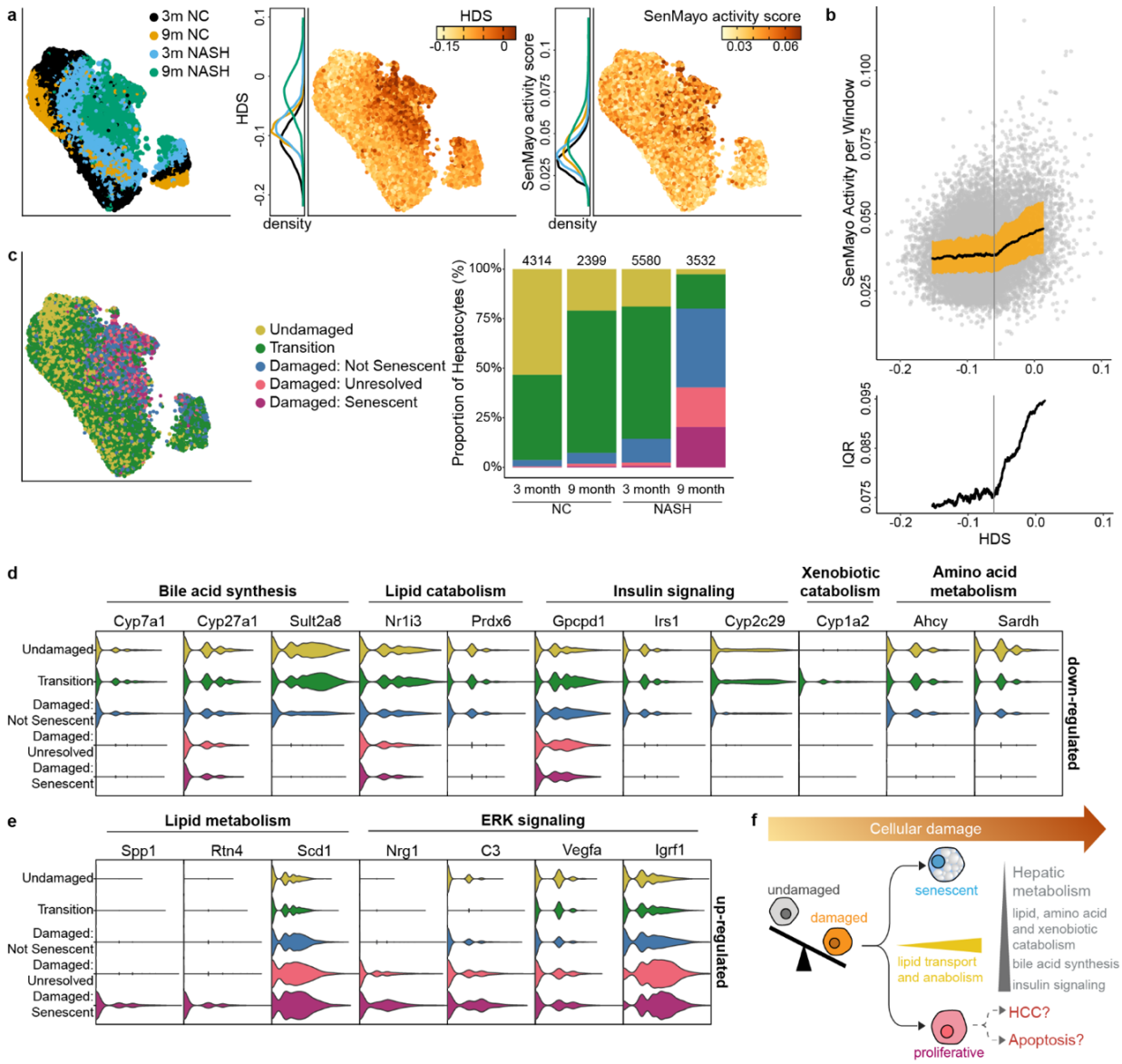

Figure 5: Analysis of hepatocyte cell fate decisions.

a. UMAP of merged snRNA-seq datasets, representing 3- and 9-month-old mice fed either NASH-inducing or normal chow (NC) diet (subset and annotated from[52]). Left: UMAP of hepatocytes colored by condition. Middle: hepatocytes colored by HDS. Right: Hepatocytes colored by SenMayo activity score. 3m = 3-month-old, 9m = 9 months-old, NC = normal chow, NASH = NASH-inducing diet. Density curves of HDS and SenMayo activity score are shown per condition, color of line represents condition.

b. SenMayo activity score versus HDS (same data as in a). Top: SenMayo activity score for each cell. Solid line: sliding window median SenMayo score calculated for 1000 hepatocytes ordered by HDS in each window. Orange: interquartile range (IQR). The data is heteroscedastic (Breusch-Pagan test, $p < 2.2 \times 10^{-16}$). Bottom: IQR per sliding window (y-axis) plotted against mean HDS per sliding window.

c. Left: UMAP as shown in a, colored by cell fate classification. Right: relative abundance of hepatocytes of each cell fate per condition. Numbers above stacked bars show the total number of hepatocytes analyzed per sample.

d. Gene expression of selected genes from a group of 210 genes differentially down-regulated in damaged-senescent hepatocytes compared to damaged-not-senescent hepatocytes.

e. Gene expression of selected genes of a total of 37 significantly differentially up-regulated genes in damaged-senescent-like hepatocytes compared to damaged-not-senescent-like hepatocytes.
f. Schematic model of hepatocyte cell fate transitions. Accumulating damage leads to loss of cellular homeostasis driving hepatocytes into different pathological cell fate trajectories. Regardless of cell fate, an increase of damage correlates with the increased expression of genes related to lipid transport and lipid anabolism that promote steatosis. When transiting in the direction of senescence, cells show an additional downregulation of genes involved in defining metabolic functions of hepatocytes such as amino acid and xenobiotic catabolism, insulin signaling, and bile acid synthesis. In parallel genes involved in lipid catabolism are downregulated, thereby further exacerbating lipid accumulation in senescent cells.

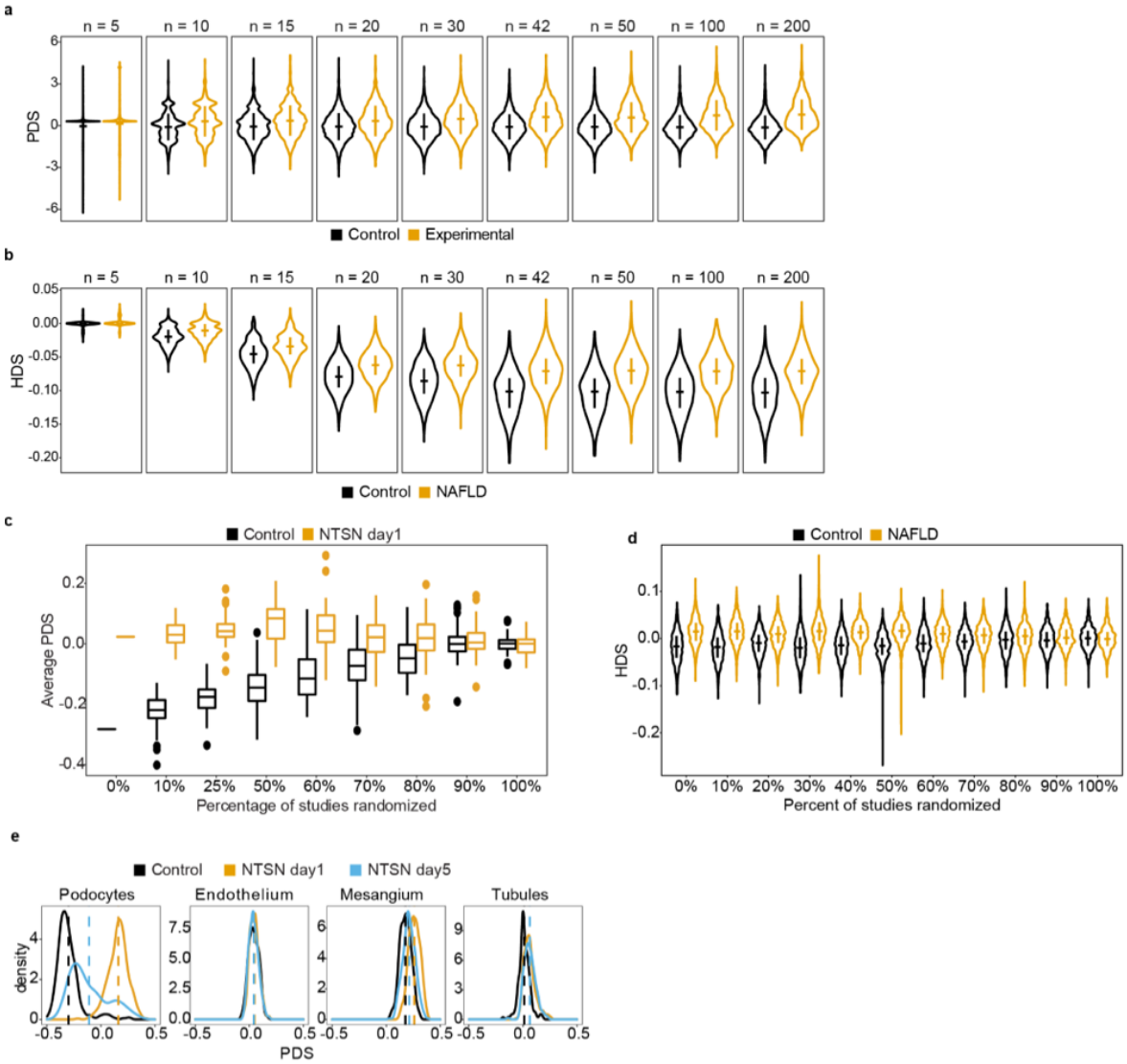

Supplementary Figure 1: Robustness and specificity of PDS and HDS.

a. Robustness of the podocyte damage score was tested for varying gene signature sizes. Three novel snRNA-seq (Wt1$^{ko/wt}$, Nphs2^{mut}, Pdss2^{mut}) and four public scRNA-seq datasets[55] were used to test for the number of genes in the PDS needed to robustly differentiate control (black) and experimental (orange) conditions. PDS were scaled per study (Y-axis). Number of top genes (*n*) used per signature is indicated above. Insets in violin plots show the mean plus/minus 2 standard deviations, also in panels b and d.
b. Same as in *a* for HDS, except HDS is not scaled. Median HDS per distribution are indicated; whiskers represent the IQR. HDS calculated for snRNA-seq of hepatocytes from 24-week-old mice with and without NFLD-inducing diet (data from Liver Cell Atlas, GSE192742[9,48]).
c. PDS robustness test against noise in training data. Varying fractions of the training data were randomized to test how this would reduce the ability of the PDS to successfully distinguish experimental from control conditions in independent test data (see Methods). scRNA-seq data from nephrotoxic serum nephritis (NTSN) model of podocyte damage[55] was used for the test. 50 rounds of randomization were conducted for each 'percentage of studies randomized'. Box plots show first (Q1), second, and third quartiles (Q) of the distribution of average PDS per cell across 50 randomization rounds per

‘percentage randomized’. Whiskers represent Q1 - 1.5 x interquartile range (IQR) and Q3 + 1.5xIQR. Outlier cells are represented by dots.

d. Same as in c, but for the HDS. Test was conducted on hepatocyte snRNA-seq data from 24-week-old mice fed with standard (control) or Western (NAFLD) diet from the Liver Cell Atlas (same data as in b). HDS per centered per run. Median HDS per distribution is indicated; whiskers represent IQR.
e. Cell-type specificity test. Panels show distribution of PDS (X-axis) in four major glomerular cell types (podocytes, endothelium, mesangium and tubules, color of lines reflect experimental condition (control and two damage time points). scRNA-seq data from the nephrotoxic nephritis model[55].

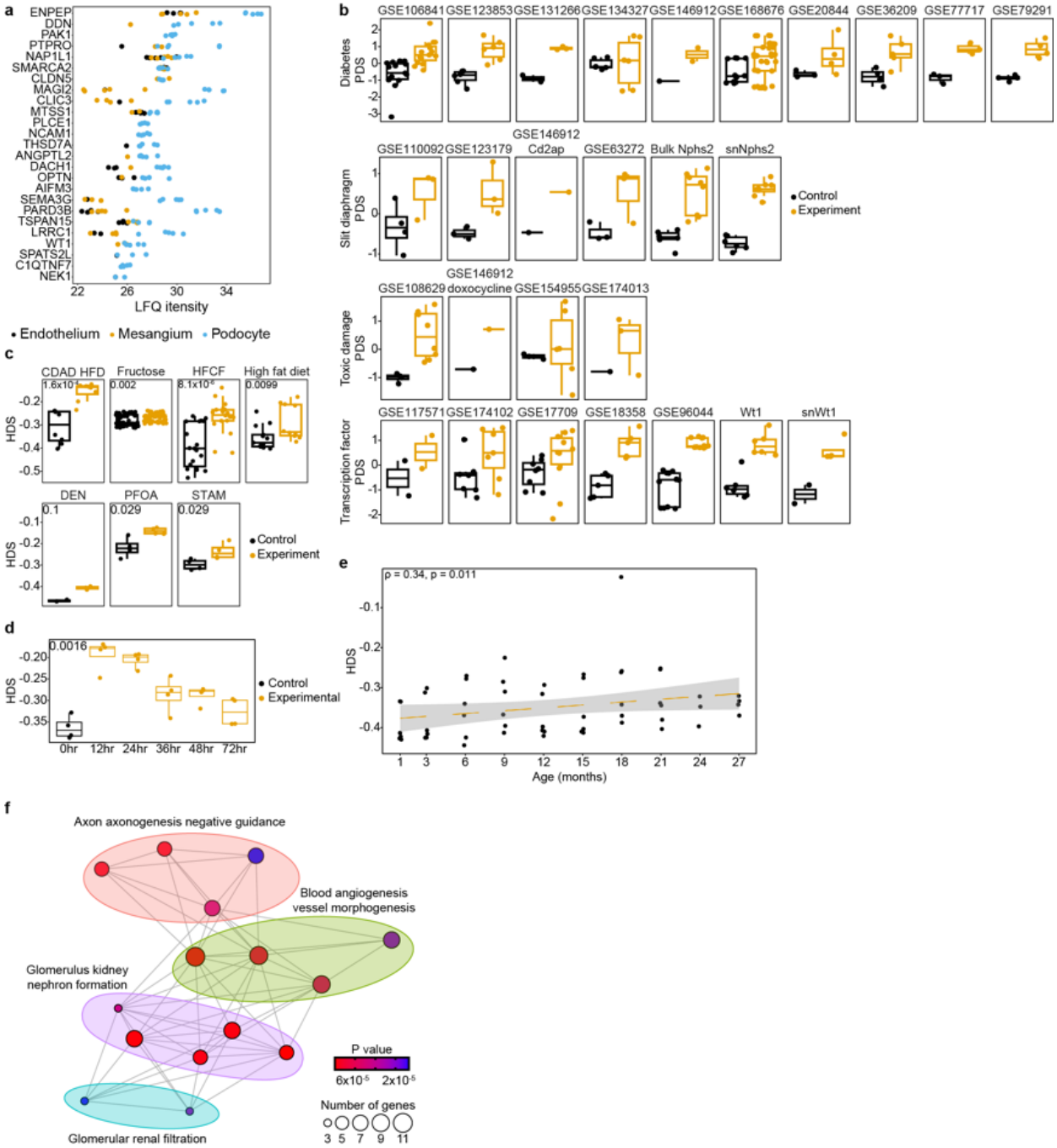

Supplementary Figure 2: Cross validation of PDS and HDS

a. Protein expression of PDS marker genes in 3 types of mouse glomerular cells: podocytes (blue), endothelial cells (black) and mesangial cells (orange). Data is from glomerular proteomics as reported in PXD016238[13]. Non-scaled protein expression values (LFQ) plotted for each gene separately.

b. Leave-one-dataset-out cross validation of the PDS. Each dataset of the indicated group of disease models were left out during the training phase of the PDS and used for testing the indicated disease models afterwards. Each dot represents the mean score across all cells of a sample, scores are scaled and centered per study. Boxplots show first (Q1), second, and third quartiles (Q) of the distribution.

Whiskers represent Q1 - 1.5 x interquartile range (IQR) and Q3 + 1.5xIQR. Outlier cells are represented by dots.

c. Leave-one-model-out cross validation of the HDS. Procedure is the same as in b. Each dot represents the HDS of one sample. CDAD HFD: choline-deficient, L-amino acid-defined, high-fat diet, HFCF: high fat, cholesterol, and fructose diet, DEN: Diethylnitrosamine (DEN)-induced carcinogenic liver injury, PFOA: perfluorooctanoic acid, STAM: mouse model that recapitulates human NASH progression to HCC and uses a combination of streptozotocin and high fat diet. Boxplots show the first (Q1), second, and third (Q3) quartiles of distribution. Whiskers show Q1 - 1.5xIQR and Q3 + 1.5 x IQR. P-values of Wilcoxon rank test (experimental versus control conditions) are shown.

d. Leave-one-model-out cross validation of the HDS. Procedure is the same as in b. Each dot represents a sample in time series murine liver samples post hepatic injury induced by acetaminophen administration (GSE111828[121]). Labels on x-axis represent the time in hours (hr) after acetaminophen administration. Untreated control samples are labeled with 0hr. P-value of Kruskal Wallis test shown.

e. Leave-one-model-out cross validation of HDS. Procedure is same as in b. Each dot represents the HDS of a murine liver sample of an age group (in months on x-axis) from the Tabula Muris Senis data set (GSE132040[122,123]). Linear regression of HDS predicted by age depicted by orange line with confidence internal as gray shading. Spearman correlation coefficients on left upper corner.

f. Functional annotation of the podocyte damage marker set confirms its relations to the key podocyte functions. GO terms were grouped by semantic similarity. Nodes are colored by p-value of Fisher's exact test and sized by the number of genes tested.

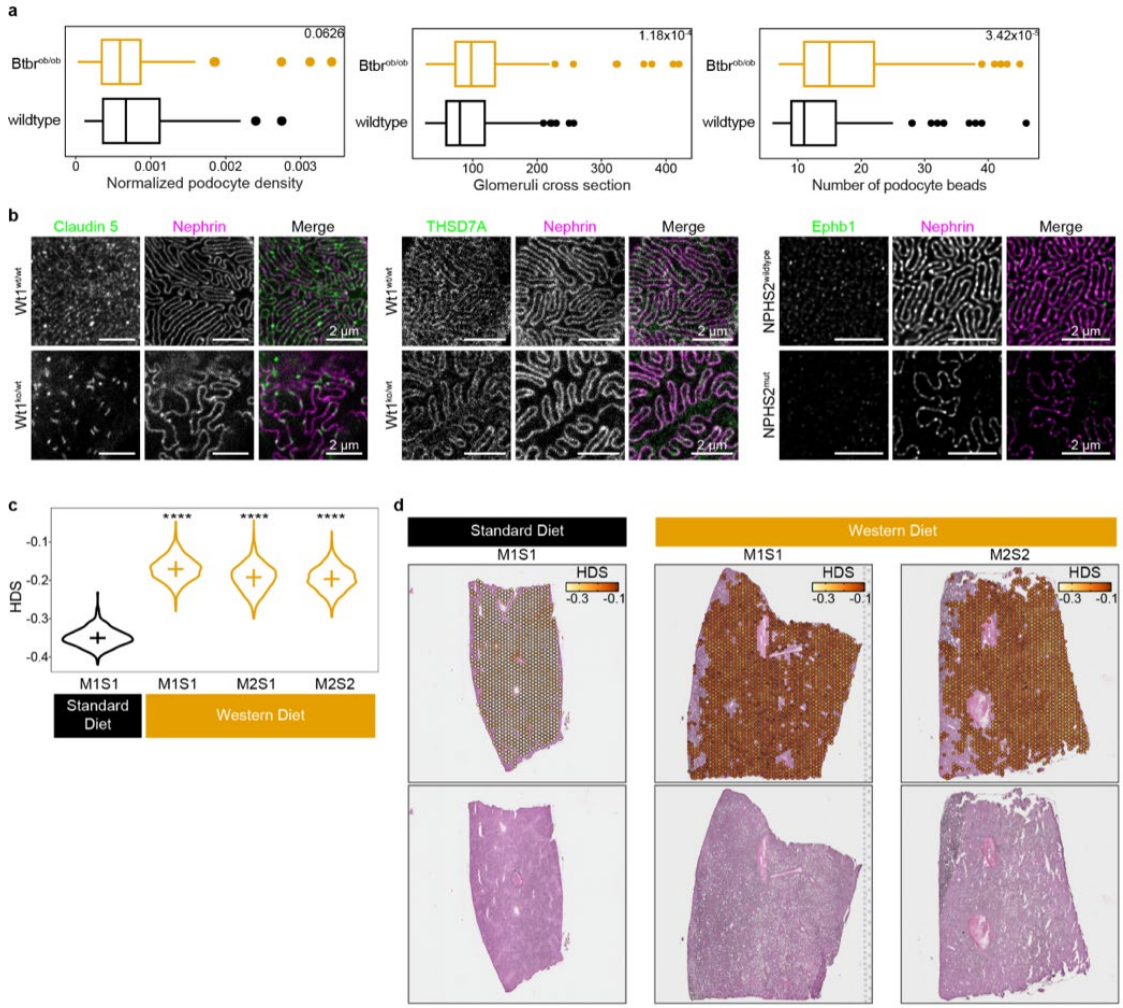

Supplementary Figure 3: Functional validation of PDS and HDS

a. Boxplots showing glomerular size estimates, podocyte bead number, and normalized podocyte density for diabetic Btbr$^{ob/ob}$ (orange) and control mice (black) as calculated on Slide-seqV2 spatial transcriptomics data provided in GSE190094[45]. Podocyte KNN filtration, glomerular identification and size estimation was performed using the programming code of the original publication[45]. Boxplots show quartiles (Q), with whiskers representing Q1 - 1.5 x interquartile range (IQR) and Q3 + 1.5xIQR. Outlier cells are represented by dots. Values in top right are p-values of Wilcoxon rank sum test of the difference between experimental and control groups.

b. STED of 12-week-old Wt1$^{ko/wt}$ or control mice co-stained for nephrin to visualize the slit diaphragm and PDS marker proteins including Claudin 5 and THSD7A. STED of 4-week-old NPHS2^{mut} or control mice was co-stained for nephrin and Ephrin B1. All PDS marker proteins localizes to the slit diaphragms. In Wt1$^{ko/wt}$ mice, Claudin 5 forms aggregates at the slit diaphragms. In NPHS2^{mut} mice, the expression of ephrin B1 is downregulated under podocyte damage.

c. Violin plots of HDS distribution in all spatial transcriptomic Visium samples from Liver Cell Atlas. M1S1 = Mouse 1 Sample 1, M2S1 = Mouse 2 Sample 1, M2S2 = Mouse 2 Sample 2. Horizontal lines show the median and vertical lines the IQR of the distributions. Wilcoxon rank sum test of Western Diet samples against M1S1. P-values = 0 depicted by ****.

d. Spatial plots of HDS distribution in spatial transcriptomic Visium samples from Liver Cell Atlas not previously shown in Fig. 1. Color range: floor = -0.37, ceiling = -0.09

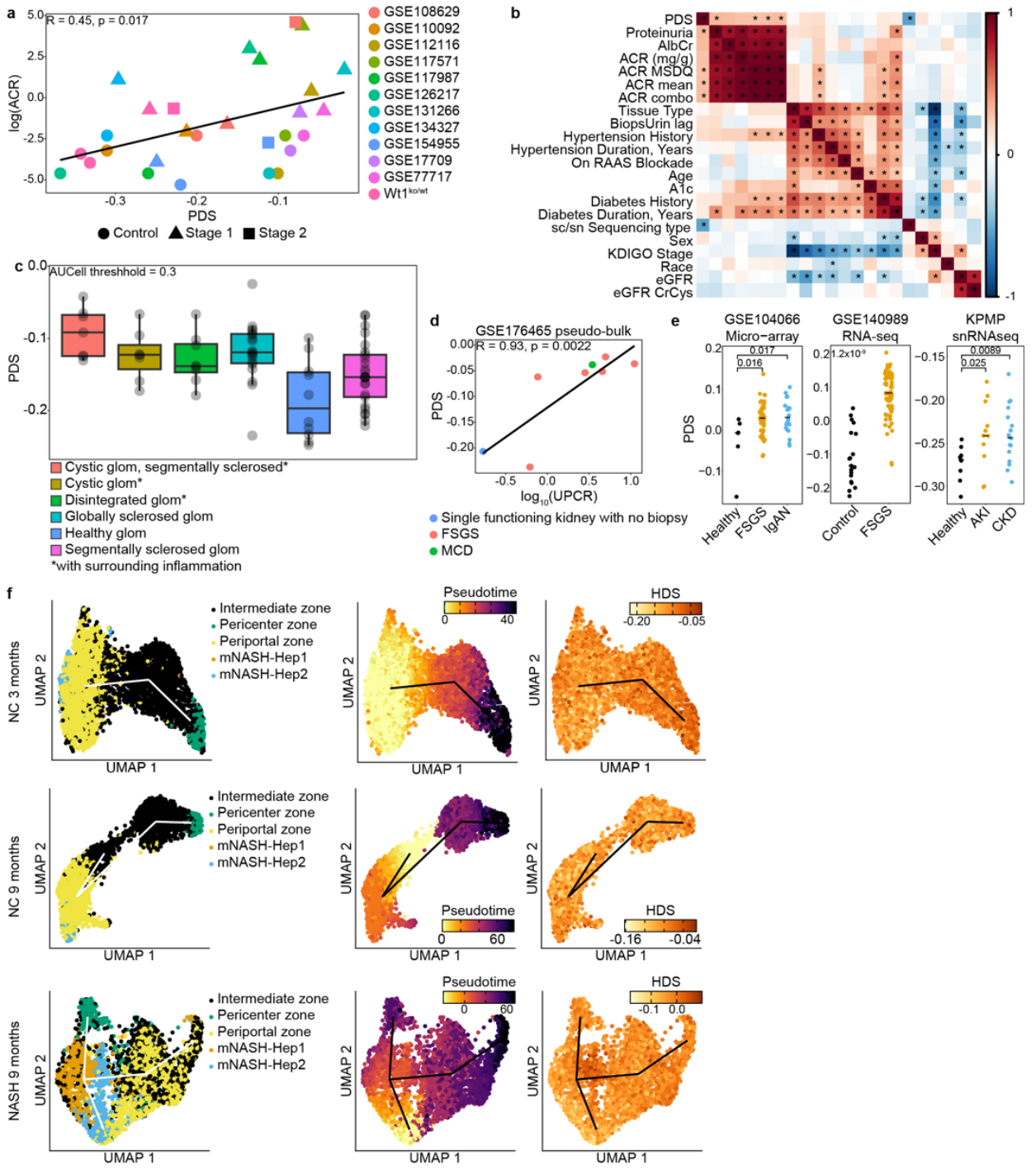

Supplementary Figure 4: Functional validation of PDS and HDS on human and mouse data

a. Correlation of urinary albumin/creatinine ratio (ACR) and PDS in bulk microarray and bulk RNA-seq data. Wt1$^{ko/wt}$ represents bulk RNAseq data published[124]. Stage 1 and 2 indicate datasets, in which longitudinal ACR data was available. Heatmap of spearman correlation between PDS and clinical traits from patients with acute kidney injury (AKI) and CKD. Anonymized patient data, sc/snRNA-seq data used in the analysis are taken from KPMP databank. Stars denote cells with P-value of spearman correlation < 0.05.

b. Boxplot shows PDS in further glomeruli as annotated manually in the histology image shown in Fig. 2b, PDS measurements based on KPMP spatial transcriptomics dataset, patient ID 29-10282.
c. Relationship between PDS calculated on human urinary podocyte snRNA-seq data and urinary protein creatinine ratio (UPCR) in patients suffering from either minimal change disease (MCD) or focal and segmental glomerulosclerosis (FSGS) as reported in GSE176465. Data from 8 patients with at least three measured podocytes each was used.
d. Validation of PDS on human transcriptomic data obtained from patients suffering from FSGS, IgA nephropathy (IgAN), acute kidney injury (AKI), and chronic kidney disease (CKD). Samples were acquired and reported in transcriptomic modalities and studies as indicated on top of the plots. Podocytes from snRNA-seq datasets were aggregated in pseudo-bulk samples. P-values of Wilcoxon rank sum test comparing experimental and control samples are shown above the points.
e. Analysis of HDS versus pseudo-time trajectories. UMAPs show hepatocytes of a 9-month-old mouse fed NASH inducing diet (same data as in Fig. 2f). Each dot represents a hepatocyte colored either by liver zone (right), PT (middle) and HDS (left). Hepatocyte zone annotation from original publication[52]. MNASH-Hep1/2: classification from original publication corresponding to damaged hepatocytes whose zone of origin could not be determined according to the authors. PT is dominated by liver zonation, while the HDS is independent of it. Top: Normal Chow 3-month-old, middle: NASH-inducing diet 9-month-old, bottom: Normal Chow 9-month-old mouse.

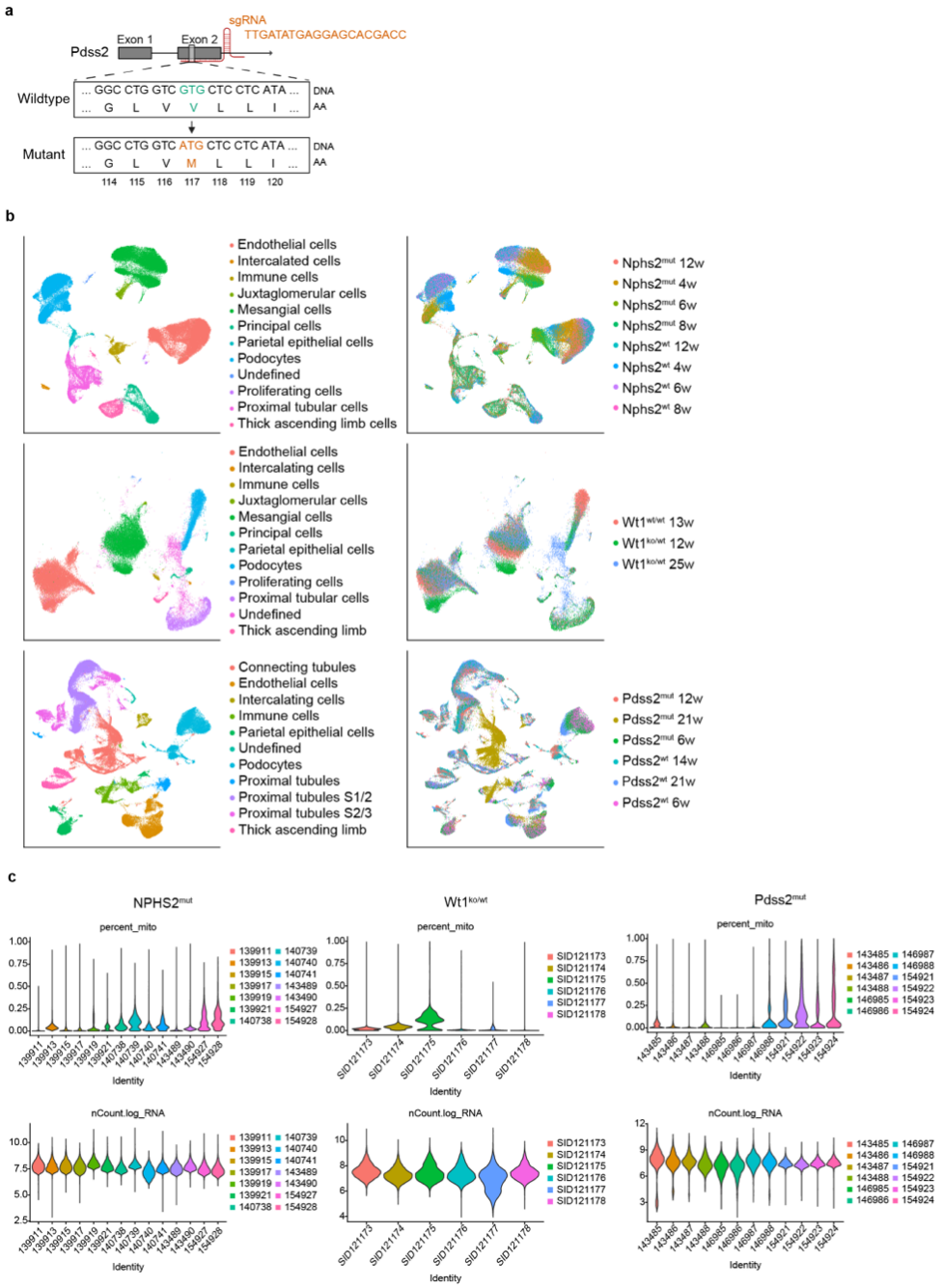

Supplementary Figure 5: Glomerular snRNA-seq were generated for Nphs2^{mut}, Wt1$^{ko/wt}$ and Pdss2^{mut} mice.

a. CRISPR strategy for the generation of the Pdss2^{mut} mice. Exon 2 of Pdss2 was targeted using single guide RNA (sgRNA) to generate a point mutation which exchanges valine (V) at amino acid (AA) position 117 to methionine (M).

b. UMAP of preprocessed snRNA-seq data colored by cell types (left) or condition (right) of NPHS2^{mut} (top), Wt1$^{ko/wt}$ (middle) or Pdss2^{mut} (bottom) datasets. UMI counts corrected for ambient RNA, filtered and normalized, as described in the Methods, were used for this and the next panels.

c. Percent mitochondria (top) and log transformed number of RNA counts (bottom) for individual snRNA-seq samples of NPHS2^{mut} (left), Wt1$^{ko/wt}$ (middle) or Pdss2^{mut} (right) datasets.

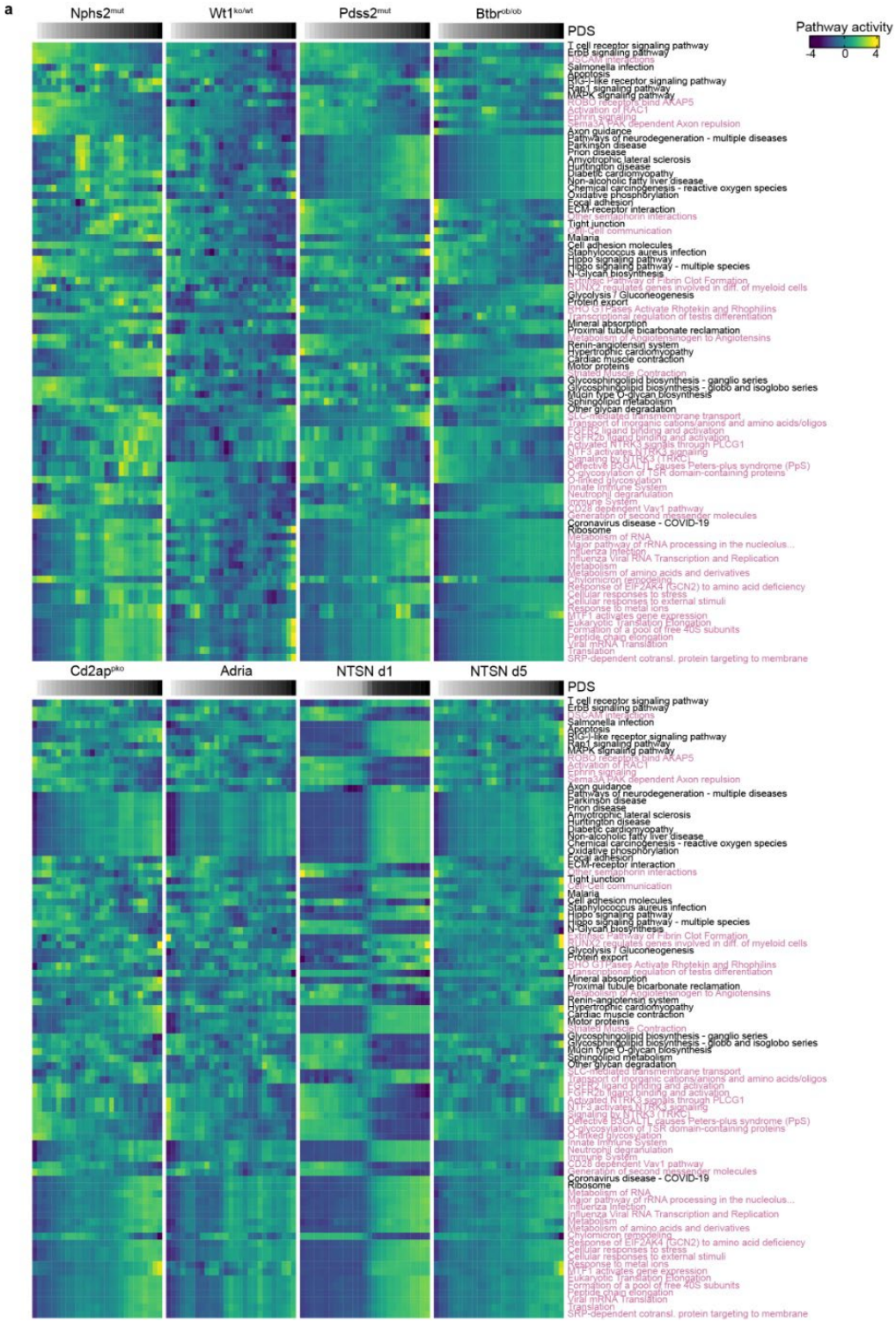

Supplementary Figure 6: Pathway fingerprints of all FSGS sc/sn-RNA-seq models

a. Cells are sorted by PDS (X-axis, PDS is increasing from left to right) and colored by activity of specific pathways (Y-axis), brighter yellow means higher activity. Pathway activity signal was smoothed. Panels show results for different FSGS models. Black and magenta colors of pathway labels denote KEGG and Reactome pathway database, respectively. A total of 85 pathways - a union of 10 pathways that most significantly (adjusted P-value < 0.05) corelate with PDS in each model - is used.

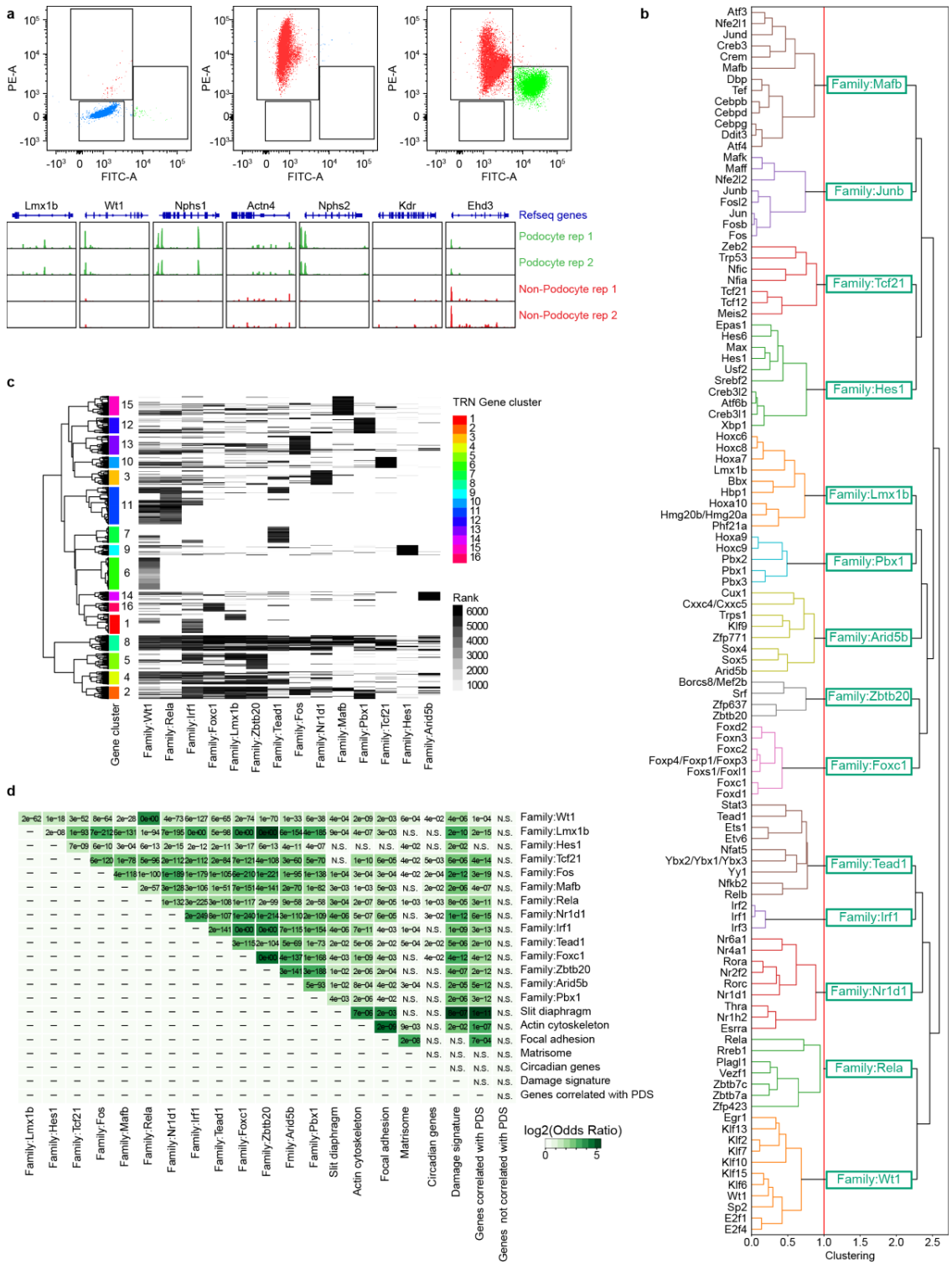

Supplementary Figure 7: Development of the podocyte-specific transcription regulatory network and identification of podocyte damage pathways.

a. Top: Fluorescence-activated cell sorting plot of glomerular nuclei extracted from nTnG;Pod:cre mice that express no nuclear fluorescence reporter (left), only tdTomato+ reporter (middle) or both GFP+/tdTomato+ reporter (right). Sorted nuclei were collected and used for the generation of cell type-

specific ATAC-seq (Methods). Bottom: genome browser tracks at podocyte-specific loci (Lmx1b, Wt1, Nphs1, Actn4, Nphs2) show accessible chromatin in podocytes, whereas those at other glomerular cell type-specific loci (Kdr, Ehd3) show accessible chromatin in non-podocytes.

b. Dendrogram of hierarchical clustering of TF motifs (PWMs). The dendrogram is cut (red line) to produce 14 TF clusters (families), each one is named by the representative motif.
c. Heatmap shows podocyte specific TRN: 14 regulatory TF-clusters (each representing a group of TFs with similar PWMs) are in columns and 6360 of their target genes expressed in podocytes are in rows. Shades of grey color shows ranks of predicted interaction score (from TFtargetCaller prediction), black and white color means the strongest and no predicted interaction, corresponding dendrogram on the left shows hierarchical clustering of genes. The dendrogram is cut to produce 16 clusters (annotated with rainbow colors), that represent common and unique targets of each of 14 regulatory modules
d. Heatmap of overlaps of 14 TF regulons and podocyte gene sets used in the Fig. 4b. Color shows log2 odds ratio of the Fisher's exact test, which represents the strength of association, cell labels show labeled with adjusted P-values of the test (if padj < 0.05, otherwise "NS").

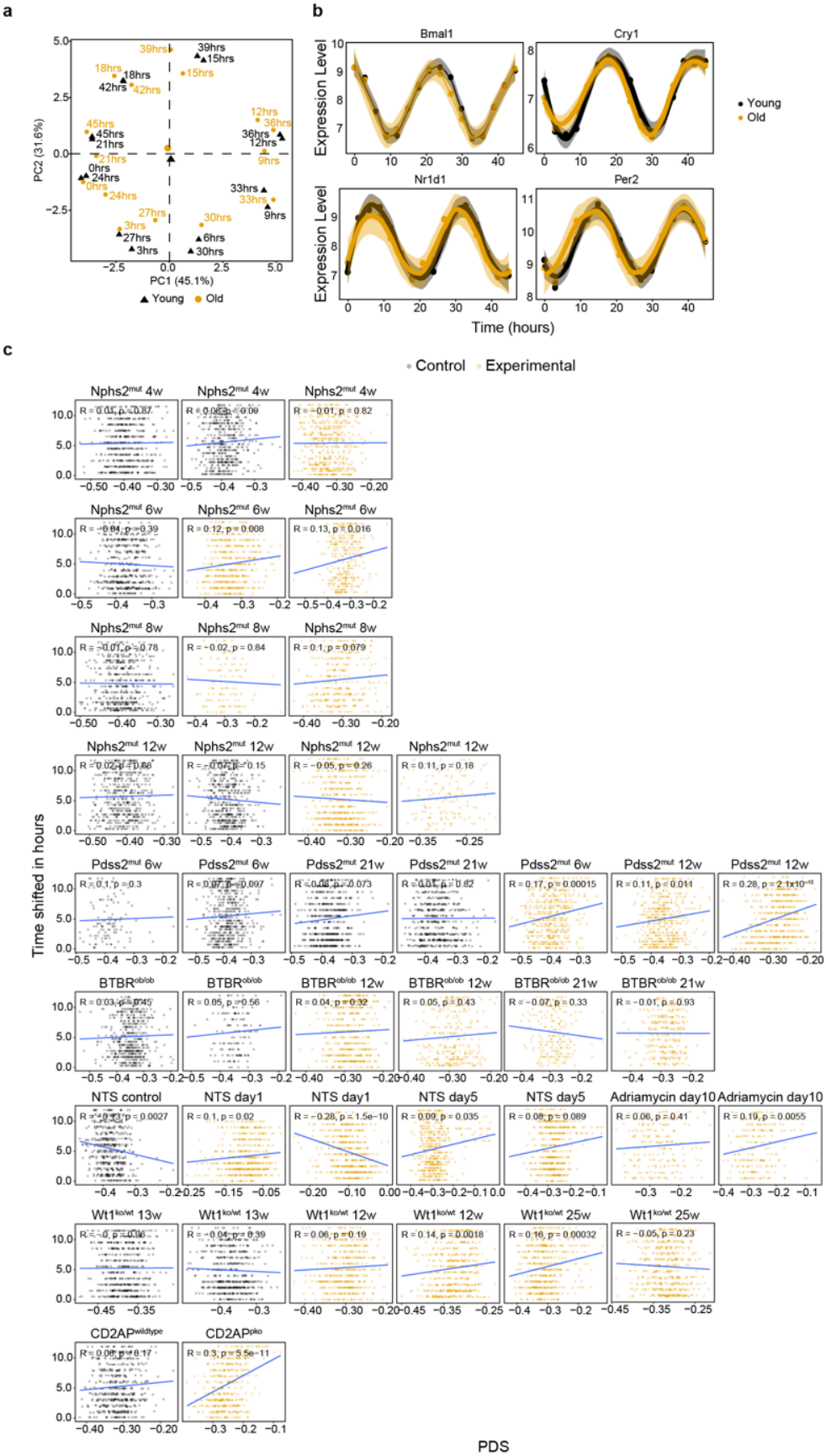
a
b
c
PC2 (31.6%)
PC1 (45.1%)
Young
Old
Bmal1
Cry1
Nr1d1
Per2
Expression Level
Time (hours)
Control
Experimental
Time shifted in hours
PDS

Supplementary Figure 8 (*prev. page*): Transcriptome analysis of circadian gene expression.

a. PCA of circadian bulk RNAseq samples from whole kidneys. Each symbol represents a pooled replicate of 3 individual mice (black: age 8 weeks, yellow: age 78 weeks). Samples were taken at zeitgeber times 0, 3, ... 21 hours during 12-h/12-h light–dark cycles. Replicates per group (n=2) are presented in serial fashion resulting in a 48h period.
b. Expression of circadian genes Bmal1, Cry1, Nr1d1, and Per2 in the same dataset as in panel a. Y-axis - gene expression value normalised by DEseq2 rlog function, X-axis – zeitgeber time, in hours. Replicates per group (n=2) are represented in serial fashion resulting in a 48h period. Solid line indicates an estimate of the conditional mean function, shades indicate 95% confidence interval of estimates. Yellow: age 78 weeks, black: age 8 wks.
c. Absolute deviation between circadian time of each cell from the reference sample time (Y-axis) of the respective sample as a function of the PDS (X-axis). Regression line and parameters for Spearman rank correlation are shown. Black and orange color of dots distinguish cells of control and experimental samples. Circadian time was calculated using a Tempo algorithm[78], Clock was used as a reference gene.

Supplementary Table 1: Disease models used for the kidney (PDS) and liver (HDS) analysis.

https://docs.google.com/spreadsheets/d/10iI-gT9rHKqAnAGcTxrU9kCCoZ_bT4z-/edit?usp=drive_link&ouid=104332495390310243054&rtpof=true&sd=true

Supplementary Table 2: Top 42 marker genes for PDS and HDS.

https://docs.google.com/spreadsheets/d/1IJTCjhsYDoTGfaw_Ix2jndaaR7Kjc9w8/edit?usp=drive_link&ouid=104332495390310243054&rtpof=true&sd=true

Supplementary Table 3: Functional characterization of top 42 HDS markers genes by GO term overrepresentation analysis.

https://docs.google.com/spreadsheets/d/1XWbiI0G_cGqRnD_IeYgK2rQDh83jcSa49aI1OvxNrAk/edit?gid=0#gid=0

Supplementary Table 4: Description of FSGS damage models and corresponding scRNA-seq datasets used in the manuscript.

https://docs.google.com/document/d/1kR1WHLUGVFdD5UfkMLIYnqQCpISb61yg/edit?usp=drive_link&ouid=104332495390310243054&rtpof=true&sd=true

Supplementary Table 5: List of 152 podocyte-specific TF target genes significantly correlated with the PDS.

https://docs.google.com/spreadsheets/d/1mDy4L6pT4ndOS_yqxGM8iz_GN7Vpt-H6/edit?usp=drive_link&ouid=104332495390310243054&rtpof=true&sd=true

Supplementary Table 6: GO term over-representation analysis of genes significantly down- or up-regulated in damaged senescent-like hepatocytes compared to damaged not-senescent-like hepatocytes.

https://docs.google.com/spreadsheets/d/1Grq4roNyS3url6QX-Huq8OVMCUZkfxO2onkTY74ASYI/edit?usp=sharing

Supplementary Table 7: Genes differentially downregulated in damaged-senescent hepatocytes compared to damaged-not-senescent hepatocytes. Only the genes passing filtering criteria are included.

https://docs.google.com/spreadsheets/d/10hyJ8VkJfIKCuw5BKN-gYMHcX_vOLdjTjxO993vG4Ow/edit?usp=sharing

Supplementary Table 8: Genes differentially upregulated in damaged-senescent hepatocytes compared to damaged-not-senescent hepatocytes. Only the genes passing filtering criteria are included.

https://docs.google.com/spreadsheets/d/1a0e2Je8OywrumdjX6BT7mtS0e1LeGbJYGPmx0BsXUBY/edit?usp=drive_link

References

1. Mills, K.T., Xu, Y., Zhang, W., Bundy, J.D., Chen, C.S., Kelly, T.N., Chen, J., and He, J. (2015). A systematic analysis of worldwide population-based data on the global burden of chronic kidney disease in 2010. Kidney Int *88*, 950–957. https://doi.org/10.1038/KI.2015.230.

2. Powell, E.E., Wong, V.W.S., and Rinella, M. (2021). Non-alcoholic fatty liver disease. Lancet *397*, 2212–2224. https://doi.org/10.1016/S0140-6736(20)32511-3.

3. Lake, B.B., Menon, R., Winfree, S., Hu, Q., Ferreira, R.M., Kalhor, K., Barwinska, D., Otto, E.A., Ferkowicz, M., Diep, D., et al. (2023). An atlas of healthy and injured cell states and niches in the human kidney. Nature *619*, 585–594. https://doi.org/10.1038/S41586-023-05769-3.

4. Mariani, L.H., Eddy, S., AlAkwaa, F.M., McCown, P.J., Harder, J.L., Nair, V., Eichinger, F., Martini, S., Ademola, A.D., Boima, V., et al. (2023). Precision nephrology identified tumor necrosis factor activation variability in minimal change disease and focal segmental glomerulosclerosis. Kidney Int *103*, 565–579. https://doi.org/10.1016/J.KINT.2022.10.023.

5. McNulty, M.T., Fermin, D., Eichinger, F., Jang, D., Kretzler, M., Burtt, N.P., Pollak, M.R., Flannick, J., Weins, A., Friedman, D.J., et al. (2022). A glomerular transcriptomic landscape of apolipoprotein L1 in Black patients with focal segmental glomerulosclerosis. Kidney Int *102*, 136–148. https://doi.org/10.1016/J.KINT.2021.10.041.

6. Hodgin, J.B., Mariani, L.H., Zee, J., Liu, Q., Smith, A.R., Eddy, S., Hartman, J., Hamidi, H., Gaut, J.P., Palmer, M.B., et al. (2022). Quantification of Glomerular Structural Lesions: Associations With Clinical Outcomes and Transcriptomic Profiles in Nephrotic Syndrome. Am J Kidney Dis *79*, 807-819.e1. https://doi.org/10.1053/J.AJKD.2021.10.004.

7. Menon, R., Otto, E.A., Hoover, P., Eddy, S., Mariani, L., Godfrey, B., Berthier, C.C., Eichinger, F., Subramanian, L., Harder, J., et al. (2020). Single cell transcriptomics identifies focal segmental glomerulosclerosis remission endothelial biomarker. JCI Insight *5*. https://doi.org/10.1172/JCI.INSIGHT.133267.

8. Ma, C., Kesarwala, A.H., Eggert, T., Medina-Echeverz, J., Kleiner, D.E., Jin, P., Stroncek, D.F., Terabe, M., Kapoor, V., ElGindi, M., et al. (2016). NAFLD causes selective CD4(+) T lymphocyte loss and promotes hepatocarcinogenesis. Nature *531*, 253–257. https://doi.org/10.1038/NATURE16969.

9. Guilliams, M., Bonnardel, J., Haest, B., Vanderborght, B., Wagner, C., Remmerie, A., Bujko, A., Martens, L., Thoné, T., Browaeys, R., et al. (2022). Spatial proteogenomics reveals distinct and evolutionarily conserved hepatic macrophage niches. Cell *185*, 379-396.e38. https://doi.org/10.1016/J.CELL.2021.12.018.

10. Mathys, H., Davila-Velderrain, J., Peng, Z., Gao, F., Mohammadi, S., Young, J.Z., Menon, M., He, L., Abdurrob, F., Jiang, X., et al. (2019). Single-cell transcriptomic

analysis of Alzheimer's disease. Nature *570*, 332–337. https://doi.org/10.1038/S41586-019-1195-2.

11. Bravo González-Blas, C., De Winter, S., Hulselmans, G., Hecker, N., Matetovici, I., Christiaens, V., Poovathingal, S., Wouters, J., Aibar, S., and Aerts, S. (2023). SCENIC+: single-cell multiomic inference of enhancers and gene regulatory networks. Nat Methods *20*, 1355–1367. https://doi.org/10.1038/S41592-023-01938-4.

12. Aibar, S., González-Blas, C.B., Moerman, T., Huynh-Thu, V.A., Imrichova, H., Hulselmans, G., Rambow, F., Marine, J.C., Geurts, P., Aerts, J., et al. (2017). SCENIC: single-cell regulatory network inference and clustering. Nature Methods 2017 14:11 *14*, 1083–1086. https://doi.org/10.1038/nmeth.4463.

13. Hatje, F.A., Wedekind, U., Sachs, W., Loreth, D., Reichelt, J., Demir, F., Kosub, C., Heintz, L., Tomas, N.M., Huber, T.B., et al. (2021). Tripartite separation of glomerular cell types and proteomes from reporter-free mice. Journal of the American Society of Nephrology *32*, 2175–2193. https://doi.org/10.1681/ASN.2020091346/-/DCSUPPLEMENTAL.

14. Yamada, H., Shirata, N., Makino, S., Miyake, T., Trejo, J.A.O., Yamamoto-Nonaka, K., Kikyo, M., Empitu, M.A., Kadariswantiningsih, I.N., Kimura, M., et al. (2021). MAGI-2 orchestrates the localization of backbone proteins in the slit diaphragm of podocytes. Kidney Int *99*, 382–395. https://doi.org/10.1016/J.KINT.2020.09.027.

15. Empitu, M.A., Kikyo, M., Shirata, N., Yamada, H., Makino, S.I., Kadariswantiningsih, I.N., Aizawa, M., Patrakka, J., Nishimori, K., and Asanuma, K. (2023). Inhibition of Importin- α -Mediated Nuclear Localization of Dendrin Attenuates Podocyte Loss and Glomerulosclerosis. J Am Soc Nephrol *34*, 1222–1239. https://doi.org/10.1681/ASN.0000000000000150.

16. Herwig, J., Skuza, S., Sachs, W., Sachs, M., Failla, A.V., Rune, G., Meyer, T.N., Fester, L., and Meyer-Schwesinger, C. (2019). Thrombospondin Type 1 Domain-Containing 7A Localizes to the Slit Diaphragm and Stabilizes Membrane Dynamics of Fully Differentiated Podocytes. J Am Soc Nephrol *30*, 824–839. https://doi.org/10.1681/ASN.2018090941.

17. Kann, M., Ettou, S., Jung, Y.L., Lenz, M.O., Taglienti, M.E., Park, P.J., Schermer, B., Benzing, T., and Kreidberg, J.A. (2015). Genome-wide analysis of Wilms' tumor 1-controlled gene expression in podocytes reveals key regulatory mechanisms. Journal of the American Society of Nephrology *26*, 2097–2104. https://doi.org/10.1681/ASN.2014090940/-/DCSUPPLEMENTAL.

18. Hinkes, B., Wiggins, R.C., Gbadegesin, R., Vlangos, C.N., Seelow, D., Nürnberg, G., Garg, P., Verma, R., Chaib, H., Hoskins, B.E., et al. (2006). Positional cloning uncovers mutations in PLCE1 responsible for a nephrotic syndrome variant that may be reversible. Nat Genet *38*, 1397–1405. https://doi.org/10.1038/NG1918.

19. Ozaltin, F., Ibsirlioglu, T., Taskiran, E.Z., Baydar, D.E., Kaymaz, F., Buyukcelik, M., Kilic, B.D., Balat, A., Iatropoulos, P., Asan, E., et al. (2011). Disruption of PTPRO causes

childhood-onset nephrotic syndrome. Am J Hum Genet *89*, 139–147. https://doi.org/10.1016/J.AJHG.2011.05.026.

20. Endlich, N., Kliewe, F., Kindt, F., Schmidt, K., Kotb, A.M., Artelt, N., Lindenmeyer, M.T., Cohen, C.D., Döring, F., Kuss, A.W., et al. (2018). The transcription factor Dach1 is essential for podocyte function. J Cell Mol Med *22*, 2656–2669. https://doi.org/10.1111/JCMM.13544.

21. Usui, T., Morito, N., Shawki, H.H., Sato, Y., Tsukaguchi, H., Hamada, M., Jeon, H., Yadav, M.K., Kuno, A., Tsunakawa, Y., et al. (2020). Transcription factor MafB in podocytes protects against the development of focal segmental glomerulosclerosis. Kidney Int *98*, 391–403. https://doi.org/10.1016/J.KINT.2020.02.038.

22. Ishibashi, R., Takemoto, M., Akimoto, Y., Ishikawa, T., He, P., Maezawa, Y., Sakamoto, K., Tsurutani, Y., Ide, S., Ide, K., et al. (2016). A novel podocyte gene, semaphorin 3G, protects glomerular podocyte from lipopolysaccharide-induced inflammation. Sci Rep *6*. https://doi.org/10.1038/SREP25955.

23. Sippl, C., Zeilbeck, L.F., Fuchshofer, R., and Tamm, E.R. (2014). Optineurin associates with the podocyte Golgi complex to maintain its structure. Cell Tissue Res *358*, 567–583. https://doi.org/10.1007/S00441-014-1968-8.

24. Sun, H., Li, H., Yan, J., Wang, X., Xu, M., Wang, M., Fan, B., Liu, J., Lin, N., Wang, X., et al. (2022). Loss of CLDN5 in podocytes deregulates WIF1 to activate WNT signaling and contributes to kidney disease. Nat Commun *13*. https://doi.org/10.1038/S41467-022-29277-6.

25. Köttgen, A., Pattaro, C., Böger, C.A., Fuchsberger, C., Olden, M., Glazer, N.L., Parsa, A., Gao, X., Yang, Q., Smith, A. V., et al. (2010). New loci associated with kidney function and chronic kidney disease. Nature Genetics 2010 42:5 *42*, 376–384. https://doi.org/10.1038/ng.568.

26. Li-Hawkins, J., Lund, E.G., Bronson, A.D., and Russell, D.W. (2000). Expression cloning of an oxysterol 7alpha-hydroxylase selective for 24-hydroxycholesterol. J Biol Chem *275*, 16543–16549. https://doi.org/10.1074/JBC.M001810200.

27. Mattow, J., Demuth, I., Haeselbarth, G., Jungblut, P.R., and Klose, J. (2006). Selenium-binding protein 2, the major hepatic target for acetaminophen, shows sex differences in protein abundance. Electrophoresis *27*, 1683–1691. https://doi.org/10.1002/ELPS.200500703.

28. Zhang, Y., Chen, X., Cao, Y., and Yang, Z. (2021). C8B in Complement and Coagulation Cascades Signaling Pathway is a predictor for Survival in HBV-Related Hepatocellular Carcinoma Patients. Cancer Manag Res *13*, 3503–3515. https://doi.org/10.2147/CMAR.S302917.

29. Ahmed, S.M.Q., Sasikumar, J., Laha, S., and Das, S.P. (2024). Multifaceted role of the DNA replication protein MCM10 in maintaining genome stability and its implication in human diseases. Cancer Metastasis Rev *43*. https://doi.org/10.1007/S10555-024-10209-3.

30. Krick, S., Shi, S., Ju, W., Faul, C., Tsai, S.Y., Mundel, P., and Böttinger, E.P. (2008). Mpv17l protects against mitochondrial oxidative stress and apoptosis by activation of Omi/HtrA2 protease. Proc Natl Acad Sci U S A *105*, 14106–14111. https://doi.org/10.1073/PNAS.0801146105.

31. Merk, M., Zierow, S., Leng, L., Das, R., Du, X., Schulte, W., Fan, J., Lue, H., Chen, Y., Xiong, H., et al. (2011). The D-dopachrome tautomerase (DDT) gene product is a cytokine and functional homolog of macrophage migration inhibitory factor (MIF). Proc Natl Acad Sci U S A *108*. https://doi.org/10.1073/PNAS.1102941108.

32. Song, J., Baek, I.J., Park, S., Oh, J., Kim, D., Song, K., Kim, M.K., Lee, H.W., Jang, B.K., and Jin, E.J. (2022). Deficiency of peroxisomal NUDT7 stimulates de novo lipogenesis in hepatocytes. iScience *25*. https://doi.org/10.1016/J.ISCI.2022.105135.

33. Kim, S.C., Kim, C.K., Axe, D., Cook, A., Lee, M., Li, T., Smallwood, N., Chiang, J.Y.L., Hardwick, J.P., Moore, D.D., et al. (2014). All-trans-retinoic acid ameliorates hepatic steatosis in mice by a novel transcriptional cascade. Hepatology *59*, 1750–1760. https://doi.org/10.1002/HEP.26699.

34. Deng, Y., Zhao, Z., Sheldon, M., Zhao, Y., Teng, H., Martinez, C., Zhang, J., Lin, C., Sun, Y., Yao, F., et al. (2024). LIFR regulates cholesterol-driven bidirectional hepatocyte-neutrophil cross-talk to promote liver regeneration. Nat Metab *6*. https://doi.org/10.1038/S42255-024-01110-Y.

35. Bartoli, D., Piobbico, D., Bellet, M.M., Bennati, A.M., Roberti, R., Della Fazia, M.A., and Servillo, G. (2016). Impaired cell proliferation in regenerating liver of 3 β-hydroxysterol Δ14-reductase (TM7SF2) knock-out mice. Cell Cycle *15*, 2164–2173. https://doi.org/10.1080/15384101.2016.1195939.

36. Hao, J.W., Wang, J., Guo, H., Zhao, Y.Y., Sun, H.H., Li, Y.F., Lai, X.Y., Zhao, N., Wang, X., Xie, C., et al. (2020). CD36 facilitates fatty acid uptake by dynamic palmitoylation-regulated endocytosis. Nat Commun *11*. https://doi.org/10.1038/S41467-020-18565-8.

37. Arai, T., Ono, Y., Arimura, Y., Sayama, K., Suzuki, T., Shinjo, S., Kanai, M., Abe, S.I., Semba, K., and Goda, N. (2017). Type I neuregulin1α is a novel local mediator to suppress hepatic gluconeogenesis in mice. Sci Rep *7*. https://doi.org/10.1038/SREP42959.

38. Verhague, M.A., Cheng, D., Weinberg, R.B., and Shelness, G.S. (2013). Apolipoprotein A-IV expression in mouse liver enhances triglyceride secretion and reduces hepatic lipid content by promoting very low density lipoprotein particle expansion. Arterioscler Thromb Vasc Biol *33*, 2501–2508. https://doi.org/10.1161/ATVBAHA.113.301948.

39. Zhang, D., Utsumi, T., Huang, H.C., Gao, L., Sangwung, P., Chung, C., Shibao, K., Okamoto, K., Yamaguchi, K., Groszmann, R.J., et al. (2011). Reticulon 4B (Nogo-B) is a novel regulator of hepatic fibrosis. Hepatology *53*, 1306–1315. https://doi.org/10.1002/HEP.24200.

40. Ma, Y., Chang, N., Liu, Y., Liu, F., Dong, C., Hou, L., Qi, C., Yang, L., and Li, L. (2021). Silencing IQGAP1 alleviates hepatic fibrogenesis via blocking bone marrow

mesenchymal stromal cell recruitment to fibrotic liver. Mol Ther Nucleic Acids *27*, 471–483. https://doi.org/10.1016/J.OMTN.2021.12.020.

41. Zoheir, K.M.A., Abd-Rabou, A.A., Darwish, A.M., Abdelhafez, M.A., and Mahrous, K.F. (2022). Inhibition of induced-hepatic cancer in vivo through IQGAP1-shRNA gene therapy and modulation of TRAIL-induced apoptosis pathway. Front Oncol *12*. https://doi.org/10.3389/FONC.2022.998247.

42. Lu, Y., Ye, Y., Bao, W., Yang, Q., Wang, J., Liu, Z., and Shi, S. (2017). Genome-wide identification of genes essential for podocyte cytoskeletons based on single-cell RNA sequencing. Kidney Int *92*, 1119–1129. https://doi.org/10.1016/j.kint.2017.04.022.

43. Berasain, C., Arechederra, M., Argemí, J., Fernández-Barrena, M.G., and Avila, M.A. (2023). Loss of liver function in chronic liver disease: An identity crisis. J Hepatol *78*, 401–414. https://doi.org/10.1016/J.JHEP.2022.09.001.

44. Wada, Y., Kidokoro, K., Kondo, M., Tokuyama, A., Kadoya, H., Nagasu, H., Kanda, E., Sasaki, T., Cherney, D.Z.I., and Kashihara, N. (2024). Evaluation of glomerular hemodynamic changes by sodium-glucose-transporter 2 inhibition in type 2 diabetic rats using in vivo imaging. Kidney Int *106*, 408–418. https://doi.org/10.1016/J.KINT.2024.05.006.

45. Marshall, J.L., Noel, T., Wang, Q.S., Chen, H., Murray, E., Subramanian, A., Vernon, K.A., Bazua-Valenti, S., Liguori, K., Keller, K., et al. (2022). High-resolution Slide-seqV2 spatial transcriptomics enables discovery of disease-specific cell neighborhoods and pathways. iScience *25*. https://doi.org/10.1016/J.ISCI.2022.104097.

46. Butt, L., Unnersjö-Jess, D., Höhne, M., Edwards, A., Binz-Lotter, J., Reilly, D., Hahnfeldt, R., Ziegler, V., Fremter, K., Rinschen, M.M., et al. (2020). A molecular mechanism explaining albuminuria in kidney disease. Nat Metab *2*, 461–474. https://doi.org/10.1038/S42255-020-0204-Y.

47. Gluchowski, N.L., Becuwe, M., Walther, T.C., and Farese, R. V. (2017). Lipid droplets and liver disease: from basic biology to clinical implications. Nat Rev Gastroenterol Hepatol *14*, 343–355. https://doi.org/10.1038/NRGASTRO.2017.32.

48. Habenicht, L.K.L., Wang, Z., Zhang, X., Li, Y., Mogler, C., Huspenina, J.S., Schmid, R.M., Weber, C., Mohanta, S.K., Ma, Z., et al. (2022). The C1q-ApoE complex: A new hallmark pathology of viral hepatitis and nonalcoholic fatty liver disease. Front Immunol *13*. https://doi.org/10.3389/FIMMU.2022.970938.

49. Brinkkoetter, P.T., Ising, C., and Benzing, T. (2013). The role of the podocyte in albumin filtration. Nat Rev Nephrol *9*, 328–336. https://doi.org/10.1038/NRNEPH.2013.78.

50. Latt, K.Z., Heymann, J., Jessee, J.H., Rosenberg, A.Z., Berthier, C.C., Arazi, A., Eddy, S., Yoshida, T., Zhao, Y., Chen, V., et al. (2021). Urine Single-Cell RNA Sequencing in Focal Segmental Glomerulosclerosis Reveals Inflammatory Signatures. Kidney Int Rep *7*, 289–304. https://doi.org/10.1016/J.EKIR.2021.11.005.

51. Mitrofanova, A., Molina, J., Varona Santos, J., Guzman, J., Morales, X.A., Ducasa, G.M., Bryn, J., Sloan, A., Volosenco, I., Kim, J.J., et al. (2018). Hydroxypropyl-β-cyclodextrin

protects from kidney disease in experimental Alport syndrome and focal segmental glomerulosclerosis. Kidney Int *94*, 1151–1159. https://doi.org/10.1016/J.KINT.2018.06.031.

52. Xiao, Y., Batmanov, K., Hu, W., Zhu, K., Tom, A.Y., Guan, D., Jiang, C., Cheng, L., McCright, S.J., Yang, E.C., et al. (2023). Hepatocytes demarcated by EphB2 contribute to the progression of nonalcoholic steatohepatitis. Sci Transl Med *15*. https://doi.org/10.1126/SCITRANSLMED.ADC9653.

53. Saelens, W., Cannoodt, R., Todorov, H., and Saeys, Y. (2019). A comparison of single-cell trajectory inference methods. Nat Biotechnol *37*, 547–554. https://doi.org/10.1038/S41587-019-0071-9.

54. Ji, Z., and Ji, H. (2016). TSCAN: Pseudo-time reconstruction and evaluation in single-cell RNA-seq analysis. Nucleic Acids Res *44*, e117. https://doi.org/10.1093/NAR/GKW430.

55. Chung, J.J., Goldstein, L., Chen, Y.J.J., Lee, J., Webster, J.D., Roose-Girma, M., Paudyal, S.C., Modrusan, Z., Dey, A., and Shaw, A.S. (2020). Single-cell transcriptome profiling of the kidney glomerulus identifies key cell types and reactions to injury. Journal of the American Society of Nephrology *31*, 2341–2354. https://doi.org/10.1681/ASN.2020020220/-/DCSUPPLEMENTAL.

56. Fukasawa, H., Bornheimer, S., Kudlicka, K., and Farquhar, M.G. (2009). Slit diaphragms contain tight junction proteins. J Am Soc Nephrol *20*, 1491–1503. https://doi.org/10.1681/ASN.2008101117.

57. Kocylowski, M.K., Aypek, H., Bildl, W., Helmstädter, M., Trachte, P., Dumoulin, B., Wittösch, S., Kühne, L., Aukschun, U., Teetzen, C., et al. (2022). A slit-diaphragm-associated protein network for dynamic control of renal filtration. Nat Commun *13*. https://doi.org/10.1038/S41467-022-33748-1.

58. Schlosser, P., Surapaneni, A.L., Borisov, O., Schmidt, I.M., Zhou, L., Anderson, A., Deo, R., Dubin, R., Ganz, P., He, J., et al. (2024). Association of Integrated Proteomic and Metabolomic Modules with Risk of Kidney Disease Progression. J Am Soc Nephrol *35*, 923–935. https://doi.org/10.1681/ASN.0000000000000343.

59. Perico, L., Conti, S., Benigni, A., and Remuzzi, G. (2016). Podocyte-actin dynamics in health and disease. Nat Rev Nephrol *12*, 692–710. https://doi.org/10.1038/NRNEPH.2016.127.

60. Schell, C., Rogg, M., Suhm, M., Helmstädter, M., Sellung, D., Yasuda-Yamahara, M., Kretz, O., Küttner, V., Suleiman, H., Kollipara, L., et al. (2017). The FERM protein EPB41L5 regulates actomyosin contractility and focal adhesion formation to maintain the kidney filtration barrier. Proc Natl Acad Sci U S A *114*, E4621–E4630. https://doi.org/10.1073/PNAS.1617004114.

61. Rogg, M., Maier, J.I., Van Wymersch, C., Helmstadter, M., Sammarco, A., Lindenmeyer, M., Zareba, P., Montanez, E., Walz, G., Werner, M., et al. (2022). a-Parvin Defines a Specific Integrin Adhesome to Maintain the Glomerular Filtration Barrier. Journal of the

American Society of Nephrology *33*, 786–808. https://doi.org/10.1681/ASN.2021101319/-/DCSUPPLEMENTAL.

62. Maier, J.I., Rogg, M., Helmstädter, M., Sammarco, A., Schilling, O., Sabass, B., Miner, J.H., Dengjel, J., Walz, G., Werner, M., et al. (2021). EPB41L5 controls podocyte extracellular matrix assembly by adhesome-dependent force transmission. Cell Rep *34*. https://doi.org/10.1016/J.CELREP.2021.108883.

63. Lv, Z., Hu, M., Fan, M., Li, X., Lin, J., Zhen, J., Wang, Z., Jin, H., and Wang, R. (2018). Podocyte-specific Rac1 deficiency ameliorates podocyte damage and proteinuria in STZ-induced diabetic nephropathy in mice. Cell Death Dis *9*. https://doi.org/10.1038/S41419-018-0353-Z.

64. Clark, A.R., Marshall, J., Zhou, Y., Montesinos, M.S., Chen, H., Nguyen, L., Chen, F., and Greka, A. (2022). Single-Cell Transcriptomics Reveal Disrupted Kidney Filter Cell-Cell Interactions after Early and Selective Podocyte Injury. Am J Pathol *192*, 281–294. https://doi.org/10.1016/J.AJPATH.2021.11.004.

65. Shi, S., Srivastava, S.P., Kanasaki, M., He, J., Kitada, M., Nagai, T., Nitta, K., Takagi, S., Kanasaki, K., and Koya, D. (2015). Interactions of DPP-4 and integrin β1 influences endothelial-to-mesenchymal transition. Kidney Int *88*, 479–489. https://doi.org/10.1038/KI.2015.103.

66. Eun Lee, J., Kim, J.E., Lee, M.H., Song, H.K., Ghee, J.Y., Kang, Y.S., Min, H.S., Kim, H.W., Cha, J.J., Han, J.Y., et al. (2016). DA-1229, a dipeptidyl peptidase IV inhibitor, protects against renal injury by preventing podocyte damage in an animal model of progressive renal injury. Lab Invest *96*, 547–560. https://doi.org/10.1038/LABINVEST.2016.34.

67. Wexler, D.J., De Boer, I.H., Ghosh, A., Younes, N., Bebu, I., Inzucchi, S.E., McGill, J.B., Mudaliar, S., Schade, D., Steffes, M.W., et al. (2023). Comparative Effects of Glucose-Lowering Medications on Kidney Outcomes in Type 2 Diabetes: The GRADE Randomized Clinical Trial. JAMA Intern Med *183*, 705–714. https://doi.org/10.1001/JAMAINTERNMED.2023.1487.

68. Mosenzon, O., Leibowitz, G., Bhatt, D.L., Cahn, A., Hirshberg, B., Wei, C., Im, K.A., Rozenberg, A., Yanuv, I., Stahre, C., et al. (2017). Effect of Saxagliptin on Renal Outcomes in the SAVOR-TIMI 53 Trial. Diabetes Care *40*, 69–76. https://doi.org/10.2337/DC16-0621.

69. Groop, P.H., Cooper, M.E., Perkovic, V., Emser, A., Woerle, H.J., and Von Eynatten, M. (2013). Linagliptin lowers albuminuria on top of recommended standard treatment in patients with type 2 diabetes and renal dysfunction. Diabetes Care *36*, 3460–3468. https://doi.org/10.2337/DC13-0323.

70. Yoon, S.A., Han, B.G., Kim, S.G., Han, S.Y., Jo, Y.I., Jeong, K.H., Oh, K.H., Park, H.C., Park, S.H., Kang, S.W., et al. (2017). Efficacy, safety and albuminuria-reducing effect of gemigliptin in Korean type 2 diabetes patients with moderate to severe renal impairment:

A 12-week, double-blind randomized study (the GUARD Study). Diabetes Obes Metab *19*, 590–598. https://doi.org/10.1111/DOM.12863.

71. Van den Berge, K., Roux de Bézieux, H., Street, K., Saelens, W., Cannoodt, R., Saeys, Y., Dudoit, S., and Clement, L. (2020). Trajectory-based differential expression analysis for single-cell sequencing data. Nat Commun *11*. https://doi.org/10.1038/S41467-020-14766-3.

72. Randles, M.J., Woolf, A.S., Huang, J.L., Byron, A., Humphries, J.D., Price, K.L., Kolatsi-Joannou, M., Collinson, S., Denny, T., Knight, D., et al. (2015). Genetic Background is a Key Determinant of Glomerular Extracellular Matrix Composition and Organization. J Am Soc Nephrol *26*, 3021–3034. https://doi.org/10.1681/ASN.2014040419.

73. Rogg, M., Maier, J.I., Dotzauer, R., Artelt, N., Kretz, O., Helmstädter, M., Abed, A., Sammarco, A., Sigle, A., Sellung, D., et al. (2021). SRGAP1 controls small rho GTPases to regulate podocyte foot process maintenance. Journal of the American Society of Nephrology *32*, 563–579. https://doi.org/10.1681/ASN.2020081126/-/DCSUPPLEMENTAL.

74. Duez, H., and Staels, B. (2009). Rev-erb-alpha: an integrator of circadian rhythms and metabolism. J Appl Physiol (1985) *107*, 1972–1980. https://doi.org/10.1152/JAPPLPHYSIOL.00570.2009.

75. Preston, R., Chrisp, R., Dudek, M., Morais, M.R.P.T., Tian, P., Williams, E., Naylor, R.W., Davenport, B., Pathiranage, D.R.J., Benson, E., et al. (2024). The glomerular circadian clock temporally regulates basement membrane dynamics and the podocyte glucocorticoid response. Kidney Int. https://doi.org/10.1016/J.KINT.2024.10.016.

76. Wang, L., Tian, H., Wang, H., Mao, X., Luo, J., He, Q., Wen, P., Cao, H., Fang, L., Zhou, Y., et al. (2024). Disrupting circadian control of autophagy induces podocyte injury and proteinuria. Kidney Int *105*, 1020–1034. https://doi.org/10.1016/J.KINT.2024.01.035.

77. Ansermet, C., Centeno, G., Nikolaeva, S., Maillard, M.P., Pradervand, S., and Firsov, D. (2019). The intrinsic circadian clock in podocytes controls glomerular filtration rate. Sci Rep *9*. https://doi.org/10.1038/S41598-019-52682-9.

78. Auerbach, B.J., FitzGerald, G.A., and Li, M. (2022). Tempo: an unsupervised Bayesian algorithm for circadian phase inference in single-cell transcriptomics. Nat Commun *13*. https://doi.org/10.1038/S41467-022-34185-W.

79. He, L., Fan, Y., Zhang, Y., Tu, T., Zhang, Q., Yuan, F., and Cheng, C. (2022). Single-cell transcriptomic analysis reveals circadian rhythm disruption associated with poor prognosis and drug-resistance in lung adenocarcinoma. J Pineal Res *73*. https://doi.org/10.1111/JPI.12803.

80. Sanfeliu-Redondo, D., Gibert-Ramos, A., and Gracia-Sancho, J. (2024). Cell senescence in liver diseases: pathological mechanism and theranostic opportunity. Nature Reviews Gastroenterology & Hepatology 2024 21:7 *21*, 477–492. https://doi.org/10.1038/s41575-024-00913-4.

81. Saul, D., Kosinsky, R.L., Atkinson, E.J., Doolittle, M.L., Zhang, X., LeBrasseur, N.K., Pignolo, R.J., Robbins, P.D., Niedernhofer, L.J., Ikeno, Y., et al. (2022). A new gene set identifies senescent cells and predicts senescence-associated pathways across tissues. Nature Communications 2022 13:1 *13*, 1–15. https://doi.org/10.1038/s41467-022-32552-1.

82. Enooku, K., Kondo, M., Fujiwara, N., Sasako, T., Shibahara, J., Kado, A., Okushin, K., Fujinaga, H., Tsutsumi, T., Nakagomi, R., et al. (2018). Hepatic IRS1 and ß-catenin expression is associated with histological progression and overt diabetes emergence in NAFLD patients. J Gastroenterol *53*, 1261–1275. https://doi.org/10.1007/S00535-018-1472-0.

83. Cikes, D., Leutner, M., Cronin, S.J.F., Novatchkova, M., Pfleger, L., Klepochová, R., Lair, B., Lac, M., Bergoglio, C., Viguerie, N., et al. (2024). Gpcpd1–GPC metabolic pathway is dysfunctional in aging and its deficiency severely perturbs glucose metabolism. Nature Aging 2024 4:1 *4*, 80–94. https://doi.org/10.1038/s43587-023-00551-6.

84. Vizán, P., Di Croce, L., and Aranda, S. (2021). Functional and Pathological Roles of AHCY. Front Cell Dev Biol *9*. https://doi.org/10.3389/FCELL.2021.654344.

85. Zhou, S.F., Wang, B., Yang, L.P., and Liu, J.P. (2010). Structure, function, regulation and polymorphism and the clinical significance of human cytochrome P450 1A2. Drug Metab Rev *42*, 268–354. https://doi.org/10.3109/03602530903286476.

86. Wang, K., Chan, Y.C., So, P.K., Liu, X., Feng, L., Cheung, W.T., Lee, S.S.T., and Au, S.W.N. (2021). Structure of mouse cytosolic sulfotransferase SULT2A8 provides insight into sulfonation of 7α-hydroxyl bile acids. J Lipid Res *62*. https://doi.org/10.1016/J.JLR.2021.100074.

87. Dawson, P.A., and Setchell, K.D.R. (2017). Will the real bile acid sulfotransferase please stand up? Identification of Sult2a8 as a major hepatic bile acid sulfonating enzyme in mice. J Lipid Res *58*, 1033–1035. https://doi.org/10.1194/JLR.C077420.

88. Cingolani, F., Liu, Y., Shen, Y., Wen, J., Farris, A.B., and Czaja, M.J. (2021). Redundant Functions of ERK1 and ERK2 Maintain Mouse Liver Homeostasis Through Down-Regulation of Bile Acid Synthesis. Hepatol Commun *6*, 980. https://doi.org/10.1002/HEP4.1867.

89. Tang, M., Jiang, Y., Jia, H., Patpur, B.K., Yang, B., Li, J., and Yang, C. (2020). Osteopontin acts as a negative regulator of autophagy accelerating lipid accumulation during the development of nonalcoholic fatty liver disease. Artif Cells Nanomed Biotechnol *48*, 159–168. https://doi.org/10.1080/21691401.2019.1699822.

90. Sahai, A., Malladi, P., Melin-Aldana, H., Green, R.M., and Whitington, P.F. (2004). Upregulation of osteopontin expression is involved in the development of nonalcoholic steatohepatitis in a dietary murine model. Am J Physiol Gastrointest Liver Physiol *287*. https://doi.org/10.1152/AJPGI.00002.2004.

91. Zhang, S., Guo, F., Yu, M., Yang, X., Yao, Z., Li, Q., Wei, Z., Feng, K., Zeng, P., Zhao, D., et al. (2020). Reduced Nogo expression inhibits diet-induced metabolic disorders by

regulating ChREBP and insulin activity. J Hepatol *73*, 1482–1495. https://doi.org/10.1016/j.jhep.2020.07.034.

92. Pathak, G.P., Shah, R., Kennedy, B.E., Murphy, J.P., Clements, D., Konda, P., Giacomantonio, M., Xu, Z., Schlaepfer, I.R., and Gujar, S. (2018). RTN4 Knockdown Dysregulates the AKT Pathway, Destabilizes the Cytoskeleton, and Enhances Paclitaxel-Induced Cytotoxicity in Cancers. Mol Ther *26*, 2019–2033. https://doi.org/10.1016/J.YMTHE.2018.05.026.

93. Sun, Q., Xing, X., Wang, H., Wan, K., Fan, R., Liu, C., Wang, Y., Wu, W., Wang, Y., and Wang, R. (2024). SCD1 is the critical signaling hub to mediate metabolic diseases: Mechanism and the development of its inhibitors. Biomedicine & Pharmacotherapy *170*, 115586. https://doi.org/10.1016/J.BIOPHA.2023.115586.

94. Shen, W., Yang, L., Yang, Y., Wang, P., Tao, X., Shen, Y., Wang, S., and Shen, Y. (2023). PRDX6 Promotes Fatty Acid Oxidation via PLA2-Dependent PPARα Activation in Rats Fed High-Fat Diet. Antioxid Redox Signal *38*, 1184–1200. https://doi.org/10.1089/ars.2022.0065.

95. Hernandez, J.P., Mota, L.C., Huang, W., Moore, D.D., and Baldwin, W.S. (2009). Sexually dimorphic regulation and induction of P450s by the constitutive androstane receptor (CAR). Toxicology *256*, 53–64. https://doi.org/10.1016/J.TOX.2008.11.002.

96. Wang, Q., Tang, Q., Zhao, L., Zhang, Q., Wu, Y., Hu, H., Liu, L., Liu, X., Zhu, Y., Guo, A., et al. (2020). Time serial transcriptome reveals Cyp2c29 as a key gene in hepatocellular carcinoma development. Cancer Biol Med *17*, 401. https://doi.org/10.20892/J.ISSN.2095-3941.2019.0335.

97. Dong, B., Saha, P.K., Huang, W., Chen, W., Abu-Elheiga, L.A., Wakil, S.J., Stevens, R.D., Ilkayeva, O., Newgard, C.B., Chan, L., et al. (2009). Activation of nuclear receptor CAR ameliorates diabetes and fatty liver disease. Proc Natl Acad Sci U S A *106*, 18831–18836. https://doi.org/10.1073/PNAS.0909731106.

98. Oliviero, F., Klement, W., Mary, L., Dauwe, Y., Lippi, Y., Naylies, C., Gayrard, V., Marchi, N., and Mselli-Lakhal, L. (2023). CAR Protects Females from Diet-Induced Steatosis and Associated Metabolic Disorders. Cells *12*. https://doi.org/10.3390/CELLS12182218.

99. Yan, J., Chen, B., Lu, J., and Xie, W. (2014). Deciphering the roles of the constitutive androstane receptor in energy metabolism. Acta Pharmacologica Sinica 2015 36:1 *36*, 62–70. https://doi.org/10.1038/aps.2014.102.

100. MacHado, M.V., and Diehl, A.M. (2016). Pathogenesis of Nonalcoholic Steatohepatitis. Gastroenterology *150*, 1769–1777. https://doi.org/10.1053/J.GASTRO.2016.02.066.

101. Schumacher, V.A., Schlötzer-Schrehardt, U., Karumanchi, S.A., Shi, X., Zaia, J., Jeruschke, S., Zhang, D., Pavenstaedt, H., Drenckhan, A., Amann, K., et al. (2011). WT1-dependent sulfatase expression maintains the normal glomerular filtration barrier. J Am Soc Nephrol *22*, 1286–1296. https://doi.org/10.1681/ASN.2010080860.

102. Moeller, M.J., Sanden, S.K., Soofi, A., Wiggins, R.C., and Holzman, L.B. (2003). Podocyte-specific expression of cre recombinase in transgenic mice. Genesis *35*, 39–42. https://doi.org/10.1002/GENE.10164.

103. Tröder, S.E., Ebert, L.K., Butt, L., Assenmacher, S., Schermer, B., and Zevnik, B. (2018). An optimized electroporation approach for efficient CRISPR/Cas9 genome editing in murine zygotes. PLoS One *13*. https://doi.org/10.1371/JOURNAL.PONE.0196891.

104. FastQC (2015). Preprint.

105. Ewels, P., Magnusson, M., Lundin, S., and Käller, M. (2016). MultiQC: summarize analysis results for multiple tools and samples in a single report. Bioinformatics *32*, 3047–3048. https://doi.org/10.1093/BIOINFORMATICS/BTW354.

106. Dobin, A., Davis, C.A., Schlesinger, F., Drenkow, J., Zaleski, C., Jha, S., Batut, P., Chaisson, M., and Gingeras, T.R. (2013). STAR: ultrafast universal RNA-seq aligner. Bioinformatics *29*, 15–21. https://doi.org/10.1093/BIOINFORMATICS/BTS635.

107. Yang, S., Corbett, S.E., Koga, Y., Wang, Z., Johnson, W.E., Yajima, M., and Campbell, J.D. (2020). Decontamination of ambient RNA in single-cell RNA-seq with DecontX. Genome Biol *21*. https://doi.org/10.1186/S13059-020-1950-6.

108. Hao, Y., Hao, S., Andersen-Nissen, E., Mauck, W.M., Zheng, S., Butler, A., Lee, M.J., Wilk, A.J., Darby, C., Zager, M., et al. (2021). Integrated analysis of multimodal single-cell data. Cell *184*, 3573-3587.e29. https://doi.org/10.1016/J.CELL.2021.04.048.

109. Zhang, X., Smits, A.H., Van Tilburg, G.B.A., Ovaa, H., Huber, W., and Vermeulen, M. (2018). Proteome-wide identification of ubiquitin interactions using UbIA-MS. Nat Protoc *13*, 530–550. https://doi.org/10.1038/NPROT.2017.147.

110. Durinck, S., Moreau, Y., Kasprzyk, A., Davis, S., De Moor, B., Brazma, A., and Huber, W. (2005). BioMart and Bioconductor: a powerful link between biological databases and microarray data analysis. Bioinformatics *21*, 3439–3440. https://doi.org/10.1093/BIOINFORMATICS/BTI525.

111. Durinck, S., Spellman, P.T., Birney, E., and Huber, W. (2009). Mapping identifiers for the integration of genomic datasets with the R/Bioconductor package biomaRt. Nat Protoc *4*, 1184–1191. https://doi.org/10.1038/NPROT.2009.97.

112. Carvalho, B.S., and Irizarry, R.A. (2010). A framework for oligonucleotide microarray preprocessing. Bioinformatics *26*, 2363–2367. https://doi.org/10.1093/BIOINFORMATICS/BTQ431.

113. Yu, G., Wang, L.G., Han, Y., and He, Q.Y. (2012). clusterProfiler: an R package for comparing biological themes among gene clusters. OMICS *16*, 284–287. https://doi.org/10.1089/OMI.2011.0118.

114. Hao, Y., Hao, S., Andersen-Nissen, E., Mauck, W.M., Zheng, S., Butler, A., Lee, M.J., Wilk, A.J., Darby, C., Zager, M., et al. (2021). Integrated analysis of multimodal single-cell data. Cell *184*, 3573-3587.e29. https://doi.org/10.1016/J.CELL.2021.04.048.

115. Baldarelli, R.M., Smith, C.L., Ringwald, M., Richardson, J.E., Bult, C.J., Anagnostopoulos, A., Begley, D.A., Bello, S.M., Christie, K., Finger, J.H., et al. (2024). Mouse Genome Informatics: an integrated knowledgebase system for the laboratory mouse. Genetics *227*. https://doi.org/10.1093/GENETICS/IYAE031.

116. Liberzon, A., Birger, C., Thorvaldsdóttir, H., Ghandi, M., Mesirov, J.P., and Tamayo, P. (2015). The Molecular Signatures Database (MSigDB) hallmark gene set collection. Cell Syst *1*, 417–425. https://doi.org/10.1016/J.CELS.2015.12.004.

117. Bentsen, M., Goymann, P., Schultheis, H., Klee, K., Petrova, A., Wiegandt, R., Fust, A., Preussner, J., Kuenne, C., Braun, T., et al. (2020). ATAC-seq footprinting unravels kinetics of transcription factor binding during zygotic genome activation. Nat Commun *11*. https://doi.org/10.1038/S41467-020-18035-1.

118. Grant, C.E., Bailey, T.L., and Noble, W.S. (2011). FIMO: scanning for occurrences of a given motif. Bioinformatics *27*, 1017–1018. https://doi.org/10.1093/BIOINFORMATICS/BTR064.

119. Sikora-Wohlfeld, W., Ackermann, M., Christodoulou, E.G., Singaravelu, K., and Beyer, A. (2013). Assessing computational methods for transcription factor target gene identification based on ChIP-seq data. PLoS Comput Biol *9*. https://doi.org/10.1371/JOURNAL.PCBI.1003342.

120. Wu, G., Anafi, R.C., Hughes, M.E., Kornacker, K., and Hogenesch, J.B. (2016). MetaCycle: an integrated R package to evaluate periodicity in large scale data. Bioinformatics *32*, 3351–3353. https://doi.org/10.1093/BIOINFORMATICS/BTW405.

121. Bird, T.G., M ller, M., Boulter, L., Vincent, D.F., Ridgway, R.A., Lopez-Guadamillas, E., Lu, W.Y., Jamieson, T., Govaere, O., Campbell, A.D., et al. (2018). TGFβ inhibition restores a regenerative response in acute liver injury by suppressing paracrine senescence. Sci Transl Med *10*. https://doi.org/10.1126/SCITRANSLMED.AAN1230.

122. Schaum, N., Karkanias, J., Neff, N.F., May, A.P., Quake, S.R., Wyss-Coray, T., Darmanis, S., Batson, J., Botvinnik, O., Chen, M.B., et al. (2018). Single-cell transcriptomics of 20 mouse organs creates a Tabula Muris. Nature *562*, 367–372. https://doi.org/10.1038/S41586-018-0590-4.

123. Schaum, N., Lehallier, B., Hahn, O., Pálovics, R., Hosseinzadeh, S., Lee, S.E., Sit, R., Lee, D.P., Losada, P.M., Zardeneta, M.E., et al. (2020). Ageing hallmarks exhibit organ-specific temporal signatures. Nature *583*, 596–602. https://doi.org/10.1038/S41586-020-2499-Y.

124. Talyan, S., Filipów, S., Ignarski, M., Smieszek, M., Chen, H., Kühne, L., Butt, L., Göbel, H., Hoyer-Allo, K.J.R., Koehler, F.C., et al. (2021). CALINCA-A Novel Pipeline for the Identification of lncRNAs in Podocyte Disease. Cells *10*, 1–17. https://doi.org/10.3390/CELLS10030692.